This is the peer reviewed author accepted manuscript (post print) version of a published work that appeared in final form in:

Njue, Jackline CW, Salehi, Fatemeh, Lau, Timothy CW, Cleary, Matthew J, Nathan, Graham J & Chen, Longfei 2021 'Numerical and experimental analysis of poly-dispersion effects on particle-laden jets', *International Journal of Heat and Fluid Flow* vol. 91, article no. 108852, pp. 1-19

This output may not exactly replicate the final published authoritative version for which the publisher owns copyright. It is not the copy of record. This output may be used for non-commercial purposes. This version is licensed under a Creative Commons CC-BY-NC-ND 4.0 license (http://creativecommons.org/licenses/by-nc-nd/4.0/).

The final definitive published version (version of record) is available at:
https://doi.org/10.1016/j.ijheatfluidflow.2021.108852

Persistent link to the UniSA Research Outputs Repository:
http://researchoutputs.unisa.edu.au/11541.2/148274

General Rights
Copyright and moral rights for the publications made accessible in the UniSA Research Outputs Repository are retained by the authors and/or other copyright owners and it is a condition of accessing publications that users recognize and abide by the legal requirements associated with these rights.

- Users may download and print one copy for the purpose of private study or research.
- You may not further distribute the material or use it for any profit-making activity or commercial gain
- You may freely distribute the persistent link identifying the publication in the UniSA Research Outputs Repository

If you believe that this document breaches copyright, please contact us and provide details. We will remove access to the work immediately and investigate your claim.

Numerical and experimental analysis of poly-dispersion effects on particle-laden jets

Jackline C. W. Njue[1,2], Fatemeh Salehi[1,*], Timothy C. W. Lau[3,5], Matthew J. Cleary[4], Graham J. Nathan[5] and Longfei Chen[2,6,*]

[1]School of Engineering, Macquarie University, Australia

[2]School of Energy and Power Engineering, Beihang University, Beijing, China

[3]UniSA STEM, The University of South Australia, Australia

[4]School of Aerospace, Mechanical and Mechatronic Engineering, University of Sydney, Australia

[5]Centre for Energy Technology, School of Mechanical Engineering, The University of Adelaide, Adelaide, SA 5005, Australia

[6] Beihang Hangzhou Innovation Institute Yuhang, Hangzhou, China

[*]Corresponding authors: Fatemeh Salehi (fatemeh.salehi@mq.edu.au); Longfei Chen (chenlongfei@buaa.edu.cn)

Abstract

This study presents experimental measurements and computational modelling of particle-laden jets for a wide range of Stokes numbers to analyse the effect of polydispersity on particle volume fraction and velocity. The polydisperse two-phase turbulent jet issues from a pipe into a low velocity coflow, resulting in inlet Stokes numbers, St_{in}, ranging from 0.003 to 25. The particle velocity and volume fraction are experimentally measured using digital particle image velocimetry and planar nephelometry simultaneously. The simulations are conducted using a newly developed model based on the probability density function of the population balance equation (PDF-PBE) in a large eddy simulation framework. A stochastic Monte Carlo method is adopted to solve the PDF-PBE on an ensemble of notional Lagrangian particles, while the method of Stokes binning is employed to explicitly treat inertial effects in a computationally efficient way. There is a satisfactory agreement between the measurements and simulations. A series of monodisperse simulations were also conducted to compare with the polydisperse flows in a two-way coupled flow. The results confirm that in the monodisperse jet, small particles (with $St_{in} \leq 0.3$) closely follow the carrier phase velocity whereas in the polydisperse jet they are affected by the presence of larger particles to reduce their axial velocity decay rate. The opposite trend is observed for large particles ($St_{in} \geq 5.5$), confirming that in the polydisperse jet, the presence of small particles increases the large particles' radial dispersion that lowers their volume fraction along the centreline compared to the monodisperse jet.

Keywords

Polydispersity; Stokes number; particle-laden flows; PDF-PBE

1. Introduction

Particle-laden turbulent flows are relevant in natural sciences such as astrophysics, geophysics and in a wide range of engineering applications including particle solar receivers, spray coating, biomass combustion, and spray drying of food products. Particle-laden turbulent jets are an important class of particle-laden flow influencing fuel-spray interaction in a combustor (Apte et al., 2003; Mostafa et al., 1990; Oefelein et al., 2007; Zhang et al., 2004), delivery of pressurised fluid containing drugs in the respiratory tract (Cheng, 2014; Costa et al., 2016; Ma et al., 2020), interaction of air and solid particles in solid-particle solar receiver (Chen et al., 2007; Tan & Chen, 2010) and application of fire-fighting agents from fire fire-sprinkler (Gai et al., 2021; Grant et al., 2000). Therefore, understanding of the complex inter-related phenomena in particle-laden turbulent jets flows is essential to achieve significant improvements in the design of a variety of engineering devices. Such flows contain solid particles or liquid droplets suspended in a conveying fluid, and they are commonly classified as either monodisperse or polydisperse jets (Costa et al., 2016; Gai et al., 2021; Grant et al., 2000). Polydispersion is characterised by dispersed elements (that is, the solid particles or liquid droplets) having one or more properties featuring a range of values (Salehi et al., 2017) whereas monodispersion refers to the cases where all dispersed elements have identical properties. The distinction is particularly important given that while most practical systems employ polydispersed particles, current fundamental understanding of particle-laden jets is limited to cases where the particles are monodispersed. This lack of understanding is in part because the detailed, in-situ measurements of particle-laden flows require either the direct measurement of particle properties, which is challenging or requires the use of monodispersed particles (Gillandt et al., 2001; Lau & Nathan, 2014, 2016; Perrotta et al., 2020; Prevost et al., 1996). This study aims to address these challenges by utilising a combination of experimental measurements and computational modelling of a polydispersed particle-laden turbulent jet. While the measurements provide mean values averaged across all sizes, the numerical study will reveal the dynamics of particles conditional on their size.

The particle-fluid interactions can be characterised by the dimensionless Stokes number, defined as $St = \tau_p/\tau_f$ where τ_f and τ_p are the fluid characteristic time scale and the response time of physical dispersed elements to the carrier phase, respectively (Balachandar & Eaton, 2010). It is now well established that the Stokes number has a significant influence on the instantaneous particle volume fraction and velocity distributions within the flow (Aísa et al., 2002; Gillandt et al., 2001; Hardalupas, 1989; Lau & Nathan, 2014, 2016; Prevost et al., 1996; Zoltani & Bicen, 1990). In particular, in turbulent particle-laden jets two-way coupling regime, the Stokes number has been shown to impact the time-averaged particle distributions both at the pipe exit, and throughout the evolution of the jet, such that the particle volume fraction departs significantly from that of a passive scalar field (Lau & Nathan, 2016; Picano et al., 2010). For a monodisperse jet, Lau & Nathan (2016) found that the greatest variation in particle volume fraction occurred in the range of inlet Stokes number $0.3 \leq St_{in} \leq 5.6$ where the subscript "*in*" refers to the value at the inlet. While the effect of Stokes number on the distributions of particle number density and velocity in a monodisperse jet is known, there are less direct studies of the influence of Stokes numbers in a polydisperse jet.

Another important parameter characterising the particle-fluid dynamics in a particle-laden flow is the particle volume fraction, α, defined as the ratio of particle-to-fluid volumetric flow rates. In the dilute one-way coupling regime, $\alpha<10^{-6}$, the momentum exchange between the dispersed and carrier phases are small and hence the carrier phase velocity and turbulence are not affected by the dispersed

elements (Sommerfeld et al., 2008). However, at volume fractions, $\alpha > 10^{-6}$, the momentum exchange between the particles and turbulence is significant enough to alter the carrier phase and consequently the turbulence structures. This regime, called the two-way coupling regime, is particularly important given that many practical systems operate in this regime (Lau & Nathan, 2014). While there have been a number of studies on polydisperse particle-laden flows in a range of different configurations, including in turbulent boundary layers (Yarin & Hetsroni, 1994c, 1994a, 1994b), bluff-body flows (Boree et al., 2001) and jets (Prevost et al., 1996), none of them provides direct experimental measurements or simulation results on the effect of Stokes number in a turbulent, polydisperse, particle-laden jet in the two-way coupling regime.

The challenges in obtaining spatially and temporally resolved measurements in polydisperse turbulent particle-laden flows are well documented elsewhere in the literature (Varaksin & Polyakov, 1999). In laser Doppler anemometry (LDA) and phase Doppler anemometry (PDA) measurements, the signal from particles of different properties (e.g. size) are averaged within the probe volume or, where they differ too greatly, are a rejected resulting in potentially biased data. As the probe volume is typically much larger than the particle size, these challenges increase with the particle loading (Mergheni et al., 2009). Furthermore, planar measurements utilising conventional particle image velocimetry (PIV) or direct imaging of particles typically cannot reliably resolve individual particle diameters due to the use of diffraction-limited optics. These challenges are further exacerbated in the two-way coupling regime where the particle volume loadings are sufficiently large such that effects due to the overlap of particle images become significant. A combination of laser-induced fluorescence and scattering (e.g. laser-sheet drop sizing) offers a potential method to measure in-situ particle diameter (Faust et al., 2014; Lewis et al., 2020), although it has yet to be developed sufficiently to reliably overcome the challenges. While each of these measurements are capable of providing useful experimental data for a specific range of conditions and flow configurations, to the authors' knowledge there is currently no simultaneous measurements of particle velocity, number density and size in a particle-laden jet in the two-way coupling regime.

Recent advancements in computational modelling methodologies now make numerical simulations a viable option for studying the dynamics of particles in turbulent jet flows. Eulerian-Lagrangian approaches in both direct numerical simulations (DNS) and large eddy simulation (LES) are commonly adopted for such flows where the carrier phase is simulated through an Eulerian framework whereas the evolution of discrete elements' properties is dynamically tracked in a Lagrangian framework (Elghobashi, 1994; Iqbal et al., 2015; M. Kuerten, 2016). The DNS of particle-laden flows utilising the Lagrangian point-particle approach has been conducted on jet flows in the one-way and two-way coupling regimes (Freund, 2001; Sandberg et al., 2012). While these studies have advanced current understanding of particle-laden flows, they are computationally expensive and are typically limited to low Reynolds numbers. Furthermore, the smallest grid size in DNS simulations is on the order of the Kolmogorov length (M. Kuerten, 2016) and hence the DNS point particle approach is restricted to particle sizes smaller than the Kolmogorov length scale to satisfy the momentum equilibrium assumption (Jenny et al., 2012). Therefore, for larger particles with greater Stokes numbers, this causes errors as the particle size may become of the order of, or even larger than the DNS grid size where the Lagrangian point particle method is not valid anymore.

The LES-based Lagrangian point particle methods offer computationally more cost-effective approaches to predict the particle-laden flows, particularly in the two-way coupling regime. LES

methods have been demonstrated to closely match experimental data (velocity and volume fraction) in a range of particle-laden flows including in monodispersed pipes in the one-way coupling regime (Berrouk et al., 2007), and monodispersed jet two-way coupling regime (Almeida & Jaberi, 2008; Pakseresht & Apte, 2019). It has now been demonstrated that smaller particles show a weaker correlation between their mass and velocity (Berrouk et al., 2007; Pakseresht & Apte, 2019) implying that particles with greater Stokes numbers tend to maintain their initial velocity further downstream. Similar findings were reported by Barve et al. (2020) who demonstrated that the particle response to the carrier phase turbulence led to a preferential accumulation of particles, whereby the radial dispersion of the small particles is much stronger than that of particles of larger size.

A particular subclass of LES utilises a combination of the population balance equation (PBE) model (Ramkrishna, 1985; Sporleder et al., 2012) together with the probability density function (PDF) concept (Pope, 1985; Rigopoulos, 2007, 2010) to model particle-laden flows. The PBE describes the evolution of a population of particles as a function of time, space and particle properties such as particle volume and shape. The PDF-PBE model in the LES framework has also been extended to particle-laden and droplet-laden flows to explicitly consider the effects of the inertia of particles of different sizes (Salehi et al., 2017). The inertial PDF-PBE model uses an effective numerical approach, known as the method of Stokes binning, to dynamically define PDF classes that represent physical particles or droplets with similar inertial properties in bins. The model has been validated against experimental data (Salehi et al., 2017, 2018, 2019), providing confidence in its predictions of particle velocity and displacement at a lower computational cost than LES point-particle Lagrangian approaches.

Despite the recent advances in both experimental measurements and numerical modelling of particle-laden flows, there remains a lack of fundamental understanding of the dynamics of polydisperse turbulent particle-laden flows within the two-way coupling regime. More specifically, there remains a paucity of spatially-resolved, simultaneous experimental measurements of particle volume fraction, velocity and diameter that is needed to elucidate the distributions of particles of different sizes in polydispersed flows. Hence, this study aims to obtain a deeper understanding of polydisperse turbulent particle-laden flows under sufficiently dense loadings such that the particles significantly affect the gas-phase. In particular, this study will provide, for the first time, a detailed comparison between monodisperse and polydisperse jets for a wide range of Stokes numbers to understand the effect of polydispersity on the particle distributions in a turbulent jet. This will be achieved through a complementary experimental and numerical campaign. The experimental campaign will utilise PIV and planar nephelometry (PN) while the numerical modelling will utilise a hybrid LES-PDF-PBE method.

2. Methodology

2.1. Experiment Analysis

The experiment consisted of simultaneous particle image velocimetry and planar nephelometry of a turbulent, particle-laden jet issuing from a long, round, pipe into a weak co-flow, as shown in Figure 1. These experiments were identical to those previously reported by the authors (Lau & Nathan, 2016), except in the present case polydisperse rather than monodisperse particles were used. The single-phase (un-laden) velocity profiles both at the pipe exit and downstream within the jet measured by Lau & Nathan, (2016) are therefore also applicable to the current study. Details of the experimental

arrangement, equipment and imaging configuration are given in Lau & Nathan (2016), and hence only a brief overview of the experiment will be presented here.

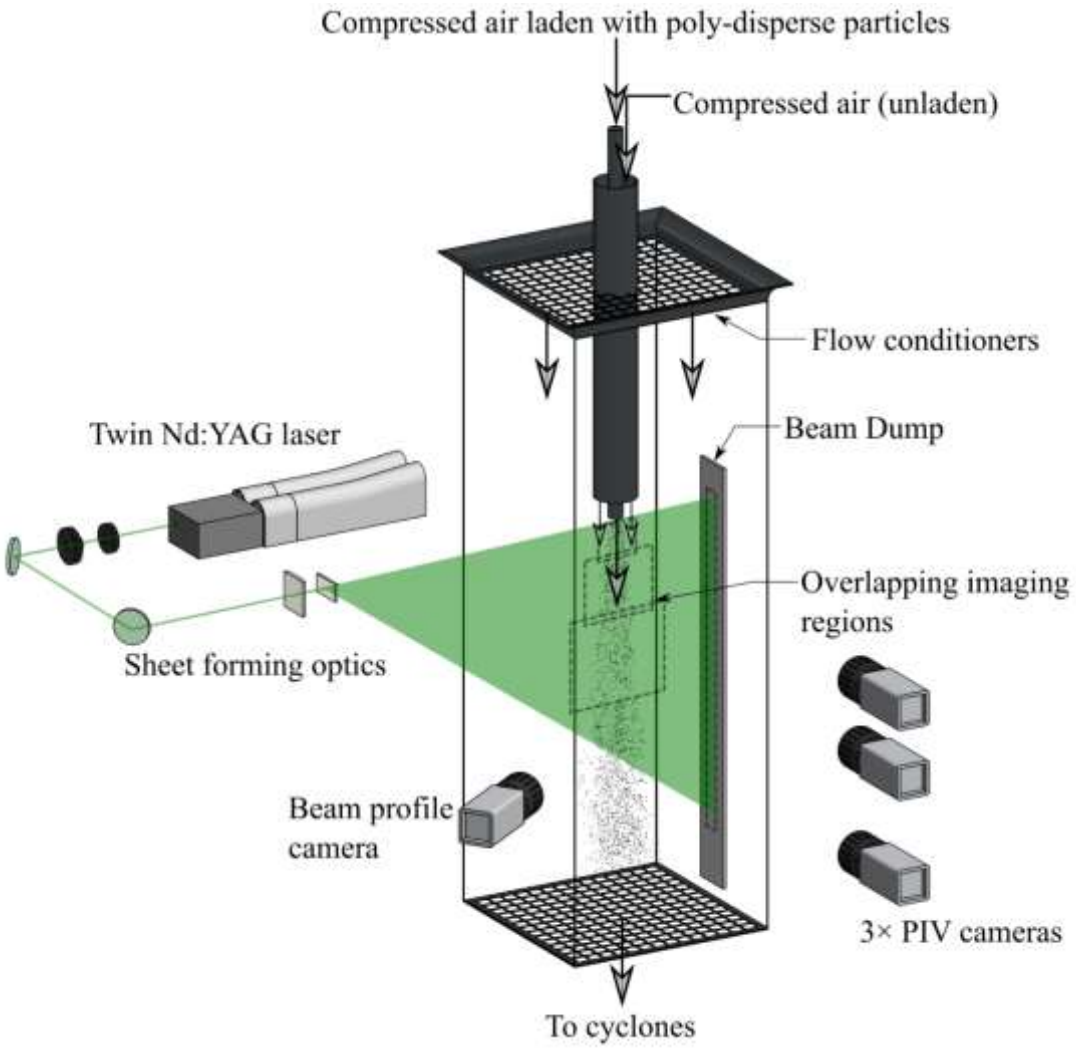


Figure 1 Schematic diagram of the experimental arrangement

As schematically shown in Figure 1, the turbulent jet is generated using a compressed air source delivered through a long, round pipe with a diameter D = 12.7 mm and a length of L = 2080 mm (L/D~164), resulting in a fully developed pipe within the pipe (Lau & Nathan, 2014). To achieve symmetry in the exit distributions of concentration and velocity, particle-laden fluid was introduced into the long pipe using two diametrically opposed circular inlets at right angles to the pipe (not shown here). The central pipe was positioned concentrically within a larger annular pipe of diameter D_{ann} = 69 mm. The exit plane of the larger annular pipe was positioned 60 mm upstream from the exit plane of the central nozzle. To avoid gravity bias, the annular and central pipes were mounted vertically in an open loop wind tunnel. The cross-section of the wind tunnel was 650 mm by 650 mm, while the axial distance from the jet exit plane to the downstream end of the tunnel was 1000 mm. An approximately uniform co-flow (see Lau & Nathan, 2016, for measured profiles of the co-flow) across the wind tunnel to the walls of the central pipe was achieved by matching the velocity of the co-annular jet to within 5% of the velocity of the wind tunnel. Care is taken to suppress the influence of static electricity by grounding the experimental apparatus at multiple locations. The flow exits the pipe into a weak, uniform, co-flow, forming a jet, with the jet to co-flow velocity ratio fixed as 12:1.

The bulk velocity of the pipe flow is $v_b = 12\ m/s$, resulting in an inlet Reynolds number of $Re_{in} = \rho v_b D/\mu = 10{,}000$ where ρ is the carrier gas density and μ is the fluid dynamic viscosity.

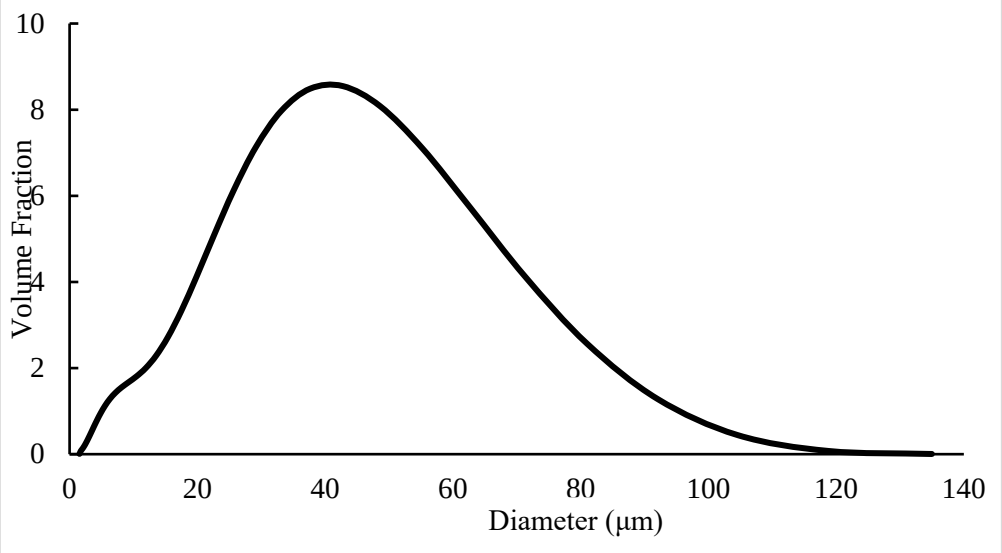


Figure 2 Particle size distribution

Polydisperse spherical glass particles with a material (absolute) density of 480 kg/m^3 were seeded into the inlet of the pipe using a carefully calibrated screw feeder. The particle-to-gas mass flow rate, i.e., the particle mass loading, is fixed at 0.4. This loading is sufficient for particle-fluid interactions to be significant, i.e., the flow was in the two-way coupling regime (Elghobashi, 2006). The particle size distribution, measured using a Malvern Mastersizer 3000, showed that the particle diameter ranged from approximately $d_d = 1.5$ to $135\ \mu m$, as shown in Figure 2. The resultant inlet Stokes number, $St_{in} = \frac{\rho_d d_d^2 v_b}{18\mu D}$, where ρ_d is the particle density, ranging from $St_{in} = 0.003$ to $St_{in} = 25$. This Stokes number range was selected because it encompasses the important regime in which particles only partially respond to the flow. That is, for Stokes number below the investigated range, $St_{in} < 0.003$, the particles are expected to follow the flow faithfully and can be therefore be treated as perfect flow tracers rather than a distinct particle phase. For Stokes number greater than the investigated range, $St_{in} > 25$, the particles are expected to approach perfect "ballistic" particles, that is, the particle phase is expected to become near-independent of the fluid phase. Additionally, these Stokes number ranges also approximately correspond to the conditions expected in practical particle-laden flows (Boree et al., 2001; Chen et al., 2007; Lau & Nathan, 2014; Tan & Chen, 2010).

Table 1 Polydisperse jet: experimental parameters

Property	Value
Particle density (ρ_d)	480 kg/m^3
Particle size (d_d)	1.5μm-135μm
Particle inlet Stokes number (St_{in})	0.003-25
Mass loading ratio	0.4
Carrier phase inlet bulk jet velocity (v_b)	12 m/s

Inlet Reynolds number (Re_{in})	10,000

A pulsed, twin head, Nd:YAG laser operating at a wavelength of 532 nm was used as the source of illumination for both PIV and PN. The laser pulsing frequency was fixed at 10 Hz. The laser beam was shaped into a thin sheet with a thickness of approximately 600 μm utilising a series of cylindrical lenses with the light sheet was aligned with the central axis of the jet. Four controllable CCD cameras (Princeton Instruments Megaplus) were employed, three to image the flow (at three different imaging regions) and one to record the beam profile downbeam of the particle-laden flow (see Figure 1). The latter camera was used to correct for effects of beam profile and attenuation through the flow, using the method developed by Kalt et al. (2007). The former three cameras were employed to image the entire radial extent of the jet from the inlet plane to 30 diameters downstream of the inlet plane. All four cameras were run under a double-frame (PIV) mode and synchronised to the light source utilising a low-jitter timing box.

Instantaneous particle velocities were derived from the raw images utilising PIV. The PIV algorithm utilises a multi-grid, multi-pass approach. The interrogation window size is 64 (streamwise) × 16 (radial) pixels for the imaging region closest to the jet inlet (corresponding to an axial distance range of 0<z/D<4), and 32 (streamwise) × 16 (radial) pixels for the remainder of the region. A 50% interrogation window overlap was applied in all cases. It should be noted that multiple particles of different diameters and velocities may be present in each interrogation window at any given time. Hence, the measured velocity is an aggregated value of the velocities of all the different particles within each interrogation window. The extent to which the range of local values of particle velocity vary about this aggregated value within the interrogation window is unknown. However, it is reasonable to expect that the aggregated velocity corresponds approximately to the area-weighted mean velocity. That is, if the particles within each interrogation window are binned into i different size bins, then for each interrogation window

$$U_m \approx \frac{\sum_i N_i d_{p,i}^2 U_i}{\sum_i N_i d_{p,i}^2} \tag{1}$$

where U_m is the measured velocity, U_i and N_i are the velocity and the number of particles with diameter $d_{p,i}$. This estimate was used because, in the absence of noise and other imaging artifacts, the strength of the PIV cross-correlation peak is approximately proportional to total cross sectional area of the particles. In practice, the measured velocity would be further biased towards larger particles. This is because larger particles have stronger scattering signals, and hence can be more reliably separated from the noise. Additionally, smaller particles tend to be more numerous, which results in particle image overlap and an overall reduction in intensity gradients. This, in turn, reduces the strength of their PIV correlation peak.

Images of the intensities of the particle light scattering are used to infer a relative particle pseudo-volume fraction. This was first done by correcting the instantaneous intensities recorded by the camera to account for background, laser beam profile and attenuation on a shot-by-shot and pixel-by-pixel basis utilising the measurements from the beam profile and the previously developed method by Kalt et al. (2007). The resultant corrected values of measured pixel intensities, *C*, are therefore

proportional to the sum of the number of particles and their cross-sectional area. If the particle images within each pixel are binned into i different size bins, therefore

$$C = K \sum_i N_i d_{p,i}^2 \tag{2}$$

where K is a constant to account for the laser power, optical transmission efficiencies and imaging parameters (see also by Kalt et al. (2007). for more details). While the value of K is unknown, it is constant for all pixels, and hence it can be normalised by, say, the centreline value at the jet inlet, C_{in} , to obtain

$$\frac{C}{C_{in}} = \frac{\sum_i N_i d_{p,i}^2}{\left(\sum_i N_i d_{p,i}^2\right)_{in}} \tag{3}$$

For cases where the turbulent flow is sufficiently well-mixed for the particle size distribution at every location within the jet to be approximately invariable, then the term $C/C_{in} \approx \theta/\theta_{in}$, where θ is the actual particle number density. However, where the range of local Stokes number spans at least two of the three regimes of particle response as is the case for the present experiment, the normalised intensity term C/C_{in} will depart from a constant value, at least on an instantaneous basis. Hence this measurement is not a true measurement of volume fraction and is termed, instead, a *pseudo* particle volume fraction. Nevertheless, despite its limitations as an absolute measurement, it is important to note that the variations in size distribution are accounted for in the numerical approach, so that the value C/C_{in}, can also be calculated with the numerical simulations. Hence this experimental measurement does provide a useful quantitative analogue that can be used for model validation.

2.2. Numerical analysis

2.2.1. Governing equations

The transport equations for the conservation of mass and momentum of the carrier phase as well as the PBE for particle number density are solved to predict the development of the particle-laden flow. While an Eulerian approach is adopted for the carrier phase, a Monte Carlo PDF version of the PBE is chosen for the dispersed phase (Salehi et al., 2017). Here the governing equations are briefly presented. The Favre filtered equations for the conservation of carrier phase mass and momentum are

$$\frac{\partial \overline{\rho}}{\partial t} + \frac{\partial \overline{\rho}\tilde{v}_i}{\partial x_i} = \tilde{S}_\rho, \tag{4}$$

$$\frac{\partial \overline{\rho}\tilde{v}_i}{\partial t} + \frac{\partial \overline{\rho}\tilde{v}_i\tilde{v}_j}{\partial x_i} = -\frac{\partial \overline{p}}{\partial x_j} + \frac{\partial}{\partial x_i}\left(\tilde{\tau}_{ij} - \tilde{\tau}_{ij}^{sf}\right) + \tilde{S}_{v_i}, \tag{5}$$

where v_i is the carrier velocity in the i-direction, p is the carrier phase pressure, S_ρ and S_{v_i} are the source terms representing the effects of the dispersed phase on the carrier phase. In this work on solid particles without interphase mass transfer, S_ρ is set to zero. The tildes denote Favre filters while the over-bars denote LES filtered values. $\tilde{\tau}_{ij}$ is the resolved viscous stress tensor and τ_{ij}^{sf} is the un-closed residual-stress tensor which is modelled using a simple eddy-viscous model (Raman & Pitsch, 2007).

The PBE governs the evolution of the instantaneous particle number density function, n, in the coordinate space, $\boldsymbol{x} = (x_1, x_2, x_3)$, and the property space, $\boldsymbol{\xi} = (\xi_1, \ldots, \xi_K)$. The PBE is written as (Sporleder et al., 2012);

$$\frac{\partial n}{\partial t} + \nabla_x(\boldsymbol{u}n) + \nabla_\xi(\dot{\boldsymbol{\xi}}n) = w \tag{6}$$

where $\boldsymbol{u}(\xi; x, t)$ is the velocity in the physical space, $\dot{\boldsymbol{\xi}}(\xi; x, t)$ is the velocity in the property space and w is the source term. In principle, the property space can include multiple properties such as particle size, shape, surface area, and morphology. However, here $\boldsymbol{\xi} = \xi_1 = \forall$ where $\forall$ is the particle volume since the focus of this study is on the dispersion of monoshaped polysized particles. In addition, $\dot{\boldsymbol{\xi}}$ and w, presenting phenomena such as surface growth, agglomeration and particle breakage, are neglected. Therefore, Eq. (6) is simplified to;

$$\frac{\partial n}{\partial t} + \nabla_x(\boldsymbol{u}n) = 0 \tag{7}$$

The PDF form of Eq. (7) is recast in a stochastic form and solved using Lagrangian notional particles in a Monte Carlo simulation. Each notional particle is a turbulent realisation of the one-time, one-point size distribution of the real physical particles. Due to significantly different slip velocities, all dispersed element sizes and trajectories cannot be represented on each notional particle. To address the significant inertial effects, the PDF-PBE is divided into classes, where each class represents the turbulent distribution of the number density function of dispersed elements that have similar inertial interactions with the carrier phase. This is achieved through the Stokes binning method (Salehi et al., 2017) which is discussed in more detail in Section 2.2.2. The stochastic differential equations for each class of notional particles can be then written as (Minier & Peirano, 2001)

$$d\boldsymbol{X} = \boldsymbol{U}dt \tag{8}$$

$$d\boldsymbol{U} = \boldsymbol{A}dt \tag{9}$$

where $\boldsymbol{X}$, $\boldsymbol{U}$ and $\boldsymbol{A}$ are the notional particle position, velocity and acceleration, respectively. Since the dominant accelerating force on the particles is the drag, the acceleration, $\boldsymbol{A}$, is written as (Maxey & Riley, 1983);

$$d\boldsymbol{U} = \frac{1}{\langle \tau_p \rangle}(\boldsymbol{v} - \boldsymbol{U})dt \tag{10}$$

where $\langle \tau_p \rangle$ is the mean response time of the PDF class due to the carrier and dispersed phase interaction forces across the class and $\boldsymbol{v}$ is the instantaneous carrier phase velocity at the particle location. Modelling of the instantaneous carrier phase velocity is first discussed followed by the discussion on the modelling of $\langle \tau_p \rangle$.

The instantaneous carrier phase velocity, $\boldsymbol{v}$ at the particle location needs to be modelled since only filtered velocities are given by the solution to Eq. (5). Comprehensive reviews of these models can be found in the works by Minier (2015), Minier et al. (2014), and Subramaniam (2013). The stochastic Langevin differential equations model the turbulent fluctuations of the gaseous flow that is seen by fluid-point particles. The solution of the Langevin equation requires models for the deterministic drift component and the stochastic diffusion component (Innocenti et al., 2016). The complexity of these models varies from simplified approaches which are based on the isotropic turbulence assumption (Pozorski & Apte, 2009) to more complex models such as the generalized Langevin models that use the PDF concept (Pope, 1985). Here, we adopt the stochastic Langevin-type model of Pozorski & Apte (2009) which has been previously applied to model turbulent particle-laden flows (Alletto &

Breuer, 2012; Riber et al., 2009; Salehi et al., 2020). The model interpolates the filtered velocity at the notional particle location from the LES solution and solves a stochastic equation for the subgrid fluctuating velocity, $\boldsymbol{v}'$ seen by particles

$$dv_i' = -\frac{v_i'}{\tau_L}dt + \sqrt{\frac{4K_{sgs}/3}{\tau_L}}d\omega_i \tag{11}$$

where K_{sgs} is the subgrid kinetic energy and $d\omega$ is an increment of the Wiener process which obeys a Gaussian distribution with zero mean and the variance equal to the size of the time step of the increment. Here, τ_L is the characteristic time scale which is obtained in directions parallel, $\tau_{L,\parallel}$, and perpendicular, $\tau_{L,\perp}$, to the direction of the relative velocity. Details on modelling τ_L can be found in (Pozorski & Apte, 2009).

2.2.2. Method of Stokes binning

The computation of $\langle\tau_p\rangle$ depends on the PDF-PBE classes that represent the physical dispersed particles with similar inertial properties. The method of Stokes binning (Salehi et al., 2017) is adopted for the selection of PDF-PBE classes. This method uses the concept of the Stokes number, $St = \tau_p/\tau_f$ that governs the inertial effects. Here, the characteristic flow time scale is computed using a characteristic eddy lifetime and hence it is defined as (Salehi et al., 2017);

$$\tau_f = \frac{\delta}{\sqrt{2K_{sgs}/3}} \tag{12}$$

In the above equation δ is the radial distance from the axis corresponding to the half-maximum of the mean axial carrier flow velocity which is obtained using the single-phase LES simulations.

The physical particle response time is modelled as (Pozorski & Apte, 2009);

$$\frac{1}{\tau_p} = \frac{1}{2}C_D\frac{\rho}{\rho_d}\frac{A_d}{\forall_d}|\boldsymbol{v}-\boldsymbol{U}| \tag{13}$$

where A_d is a reference area and $\forall_d$ is the dispersed element volume and C_D is the drag coefficient for the spherical dispersed elements computed as $C_D = 24/Re\left(1+0.15Re_p^{2/3}\right)$ where $Re_p = \rho|U-v|d_p/\mu$ (Loth, 2008). The dispersion of physical particles in a fluid depends on their Stokes number.

For $St \ll 1$, dispersed elements have small inertia and hence move with the carrier flow field whereas for $St \gg 1$, the effect of inertia is large and dispersed elements are less affected by the variations in the carrier flow. The method of Stokes binning relies on the assumption that dispersed elements within a narrow range of Stokes numbers, of width ΔSt, have approximately the same dynamic response to the carrier phase. In this method, a notional particle represents a realisation of a class of physical particles with a range of Stokes numbers, dSt, which is dynamically calculated as the flow solution evolves. Hence, the selection of PDF-PBE classes is made using the criterion of $dSt \leq \Delta St$ where ΔSt determines the maximum range of inertial responses represented by the PDF-PBE classes. This is shown schematically in Figure 3 for two notional particles, α and β, which represent realisations of the number density function of inertial elements with a range of Stokes numbers dSt_α and dSt_β, respectively. As shown in Figure 3a, for particle α, the range of Stokes numbers dSt_α is less than the

Stoke bin width ΔSt_i so that particle α satisfies the Stokes binning criterion ($dSt_\alpha \leq \Delta St_i$) and is unchanged. On the other hand, for particle β (Figure 3b), the range of Stokes numbers dSt_β is greater than the Stokes bin width ΔSt_i so that it should be split into two notional particles that satisfy the Stokes binning criterion. The resulting particles β_1 and β_2, shown in Figure 3c have an updated range of Stokes numbers, $dSt_{\beta 1}$ and $dSt_{\beta 2}$ which meet the Stokes binning criterion $dSt_{\beta 1} \leq \Delta St_i$ and $dSt_{\beta 2} \leq \Delta St_j$, respectively.

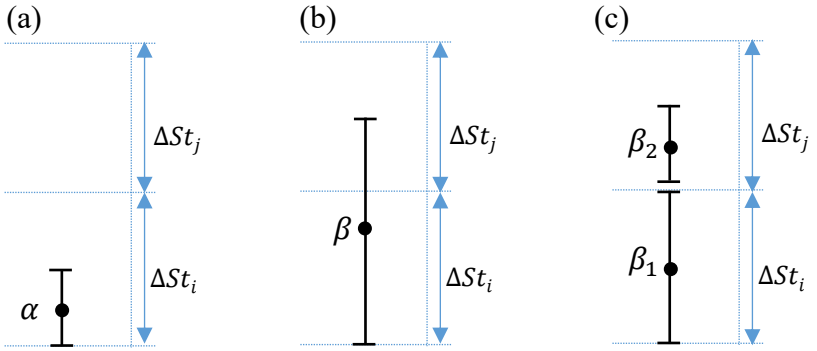


Figure 3 An illustration of the classes of probability distribution function (PDF) of particle sizes in the probility balance equation (PBE) method selection, namely (a) a distribution for particle α in which all particles are in the same Stokes regime; (b) a distribution for particle β that spans two Stokes regimes; and (c) the same case were the distribution is split into two.

The acceleration of a notional particle is then determined by the average response time, $\langle \tau_p \rangle$, which is calculated over the physical particles represented by that notional particle. At each time step, Eq. 8 and 9 are solved for notional particles to obtain their velocity and position and consequently update their dSt. If the criterion $dSt \leq \Delta St$ is satisfied, the simulation progresses to the next timestep, otherwise, the notional particle is split into two or more notional particles to ensure that their range of Stokes numbers satisfies the Stokes criterion. The model has been found to provide a great reduction in computational cost in predicting particle dispersion while maintaining its accuracy (Salehi et al., 2017, 2019). More details on the model implementation are reported by Salehi et al. (2019).

The Stokes bin size, ΔSt, is a numerical input parameter that is selected prior to simulations and its optimum value depends on the desired accuracy and availability of computational resources. Inaccurate results may be caused by very large ΔSt whereas very small ΔSt increases the computational cost. Comprehensive studies on the selection of ΔSt and numerical convergence of the Stokes binning method as ΔSt decreases have been conducted by Salehi et al. (2017). It was found that constant bin spacing in logarithmic space works best; $\Delta St = \Delta St_i = \log St_{i+1} - \log St_i$ where St_{i+1} and St_i are the bin limits for ith bin. Following the previous studies (Salehi et al., 2017, 2020), eight bins with a constant bin spacing (in logarithmic space) of $\Delta St = 0.38$ was adopted here.

2.2.3. Numerical implementation and set-up

The LES-PDF-PBE hybrid method was implemented in OpenFOAM which is a C ++ open source CFD platform. Following the architecture of the OpenFOAM classes, nested template classes are used to implement the stochastic Lagrangian solver of the PDF-PBE method to segregate the different physical processes as discussed in Salehi et al. (2020). Conservation of mass and momentum Eq. (4)

and (5) were implicitly solved using a standard spatial and temporal second-order LES solver. The Smagorinsky model is adopted for subgrid carrier phase velocities (Greenshields, 2011; Smagorinsky, 1963) where the model coefficients, C_k and C_e, are set as 0.094 and 1.048, respectively. The carrier phase velocities, density, and turbulent kinetic energy at the particle locations are computed through a tri-linear interpolation scheme from the three-dimensional finite volume fields. This is followed by solving stochastic Eqs. (8) and (9) for notional particles using a temporally first-order Euler-Maruyama scheme described in Kloeden et al. (1995). Finally, the momentum source term on the LES mesh is obtained from notional particles using the particle source in cell method.

As schematically shown in Figure 4, a cylindrical computational domain is considered to simulate the experimental test case. The jet diameter is 12.7 mm which is the same as the inner pipe diameter in the experiment whereas the domain outer diameter is reduced to 250 mm to limit computational cost. This domain outer diameter was sufficiently large to ensure that the region of interest is not disturbed by the side boundaries. The axial length of the domain is 380 mm. The mesh has approximately 2.57M hexahedra cells with a cell size of 0.2 mm at the inner jet. To ensure a good mesh quality, we follow the criterion given by Pope (1985) for LES mesh resolution and found that 99% of cells in the domain have a value of K_{res}/K larger than 0.8 where K_{res} is the resolved kinetic energy and $K = K_{res} + K_{sgs}$ is the total kinetic energy. At the inlet and outlet, zero gradient pressure and non-reflective pressure boundaries are applied, respectively. For both the main jet and co-flow, time-varying realistic turbulent velocity boundary conditions are applied. For this purpose, two pipe single-phase LES simulations are performed separately in a pre-processing step to generate realistic main jet and co-flow velocities for the simulations.

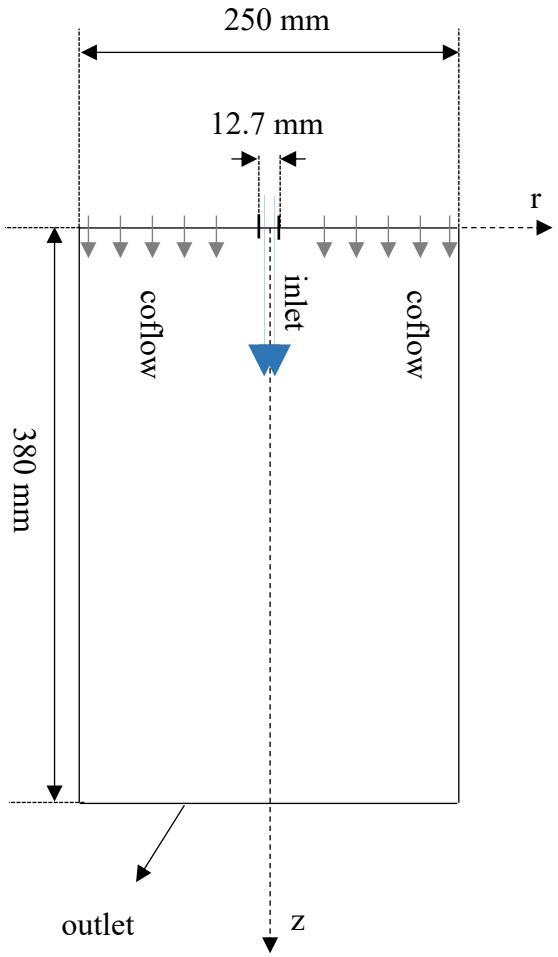


Figure 4 Computational domain

The notional particles are released at the inlet of the domain. Their x and y locations are randomly selected on the inlet patch while their z location is constant ($z = 0$). A realistic distribution of particles velocity at the inlet of the domain requires a sophisticated approach that includes extending the domain upstream of the inlet plane (i.e. the pipe exit) to inject particles within the inner pipe allowing notional particle velocities to relax to a turbulent distribution. However, this approach is computationally expensive as it requires modelling a fully developed particle-pipe flow (L = 2 m) considering particle-particle interactions and the effect of the rough pipe walls on particles. Alternatively, a simplified method is used here. Previous studies (Kirchmann et al., 2020; Salehi et al., 2020) added randomness to the particle injection velocity by imposing some levels of fluctuations to the particle injection velocity. This can be achieved by initialising notional particles with the patch (carrier gas) velocities. Here, due to the lack of velocity measurements for different particle sizes at the pipe exit (the inlet of the domain), we associate the unsteady, filtered carrier velocity to the injected notional particles at the inlet. Previous studies confirmed that this simplified method could be reasonable at least for modelling the particle velocity particularly when there is a lack of detailed measurements at the pipe exit (Kirchmann et al., 2020; Salehi et al., 2020).

Table 2 Simulation cases

Case	Jet	d_p (μm)	St_{in}

1	Polydisperse	1.5-135	0.003-25
2	Monodisperse	135.0	25
3	Monodisperse	81.02	9
4	Monodisperse	62.76	5.5
5	Monodisperse	15.41	0.3

In addition to the polydisperse case which is the same as the experimental case described in Section 2.1, we conduct a series of monodisperse jet simulations to shed light on differences in the flow field between the polydisperse and monodisperse particles. The mass loading is fixed at 0.4 for all monodisperse simulations. The list of simulations is presented in Table 2. The selected particle sizes for the monodisperse simulations ensure that the comparison is made for a wide range of St_{in}. For the polydisperse jet, an injected notional particle initially represents the entire range of glass bead sizes shown in figure 2. However, it immediately splits into as many as notional particles to ensure each notional particle represents a range of glass bead sizes such that their inlet Stokes numbers satisfy the Stokes binning criterion $dSt \leq \Delta St$. For monodisperse cases, a notional particle only represents a single glass bead size. Other case set-up and parameters for monodisperse simulations are the same as the polydisperse jet.

Statistics are collected over $70\tau_{ft}$ after the establishment of a statistically stationary flow state. τ_{ft} is a characteristic time obtained using the mean inlet velocity (12 m/s) and the domain length (380 mm) in the simulation. No significant difference in the results is observed for a longer collection period. For the polydisperse simulation, following Eq. (1) particle velocity averaged across all particle sizes are obtained by weighting the quantities of each particle size by d_p^2 (i.e., their cross-sectional area). This was done on the basis that the PIV experimental measurements would be more heavily weighted towards particles with a larger image area as discussed in Section 2.1. The mean intensity (pseudo particle volume fraction) is also computed here. As noted in Section 2.1, the current experimental setup measures the light intensity. In monodisperse jets, the particle volume fraction can be readily obtained from the intensity since the particle diameter is constant while for the polydisperse case, this is not possible. Hence, we compute the mean intensity from the simulation data and compare it with the measurement in Section 3.2.

3. Results and discussion

The simulation results and the experimental measurements are presented in this section. We first focus on the single-phase simulation (without particles) to validate the LES. This is followed by a discussion of the polydisperse jet particle data obtained using the PDF-PBE model and the experiment. Finally, a comprehensive comparison is conducted between the monodisperse and polydisperse jets to shed some light on the polydispersity effects in two-way coupling particle-laden flows. The experimental single-phase mean and root mean square (RMS) axial velocity presented in section 3.1 are the experimental measurement from Lau & Nathan, (2016) under identical conditions. The experimental particle mean and RMS axial velocity and pseudo particle volume fraction averaged across all sizes presented in section 3.2.1 are the current polydisperse jet particle experimental measurements. It

should be noted that v refers to the carrier (gas) phase velocity while U refers to the particle velocity. This is consistent with the notation in governing equations (i.e. Eqs. 4, 5, 8, and 9).

3.1. Single-phase jet

To provide a schematic view of the flow field, the contour plots of the LES single-phase mean and RMS axial velocities are shown in Figure 5. It can be seen that while the maximum mean velocity occurs along the centreline, the maximum axial velocity RMS occurs in the shear layer rejoin at both sides of the centreline. This is consistent with the radial profiles, as discussed below.

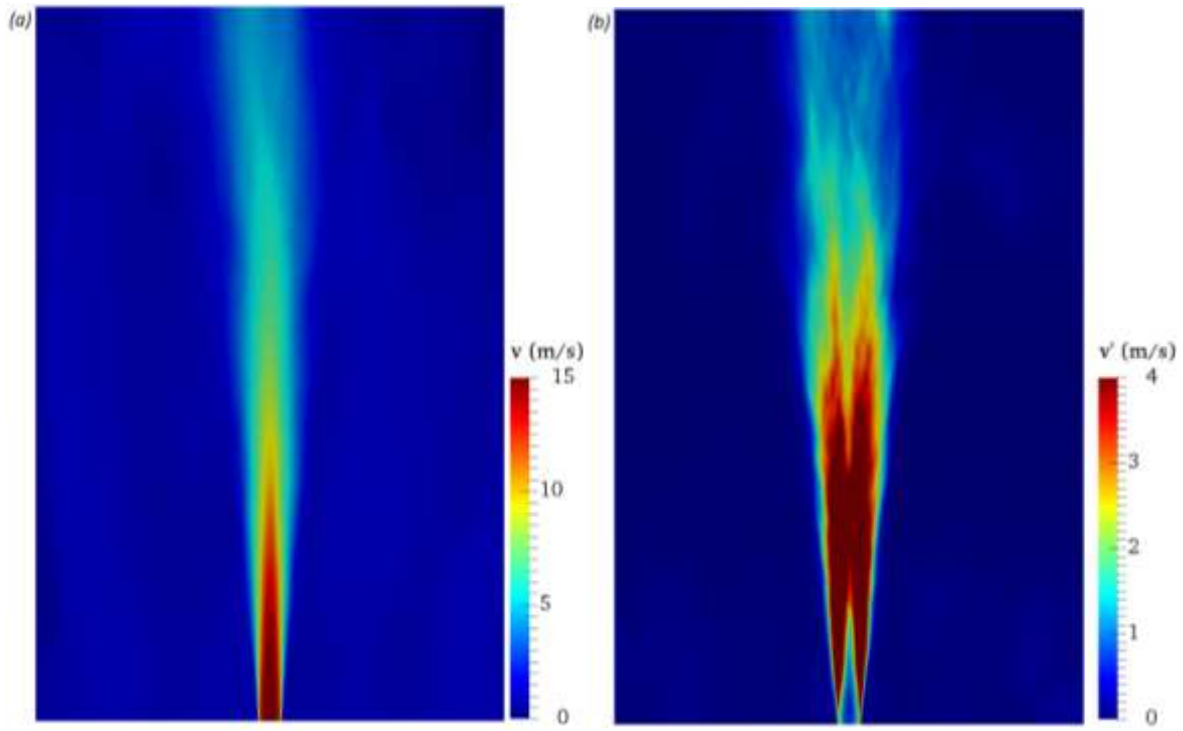


Figure 5 Color contour plot for the single-phase mean velocity and the single-phase RMS velocity. The resutls are obtained using the LES data.

Figure 6 and Figure 7 present the centreline and radial profiles (at $z/D = 10$ and 20) of the single-phase mean and RMS axial velocity obtained from the current LES. Also included are the experimental data from Lau & Nathan (2016) under identical conditions. As can be seen, the predicted values of mean velocity match the experimental data within a maximum of 5.2% difference between the two along the centreline which occurs approximately at $z/D = 10$ and negligible difference further downstream i.e. $z/D > 20$ (Figure 6a). The radial mean velocity profiles (Figure 6b and 6c) also agree well with the measured data.

The RMS velocity results of the model also show good agreement with the experimental results, with the most significant difference occurring in the near field, $1 < z/D < 4$. Further downstream, the agreement between the LES and measurements improves where the modelling results slightly underestimate the peak value of RMS velocity. The radial RMS velocity profile at $z/D = 10$ has a double bump profile, with peak values of v_{rms} occurring near to the shear layer ($|r/D| \approx 0.45$) as expected (see also contour plot shown in Fig. 5b). A similar trend is also observed in the measured data although the peak value is smaller. The ratio of the peak-to-centreline value of v_{rms} is ≈ 1.19 in

the simulations, and ≈ 1.04 in the experimental measurements. By comparison, in a similar single-phase turbulent pipe jet, a ratio of ≈ 1.09 was measured at the same axial location using hot wires (Bogusławski & Popiel, 1979). The lower value of the measurements of Lau & Nathan, (2016) is attributed to the lower spatial resolution of PIV than that of hot-wire anemometry. A lower spatial resolution results in spatial averaging of the velocity, which may result in an underestimation of v_{rms}. The overestimation of v_{rms} by the LES is possibly related to the prediction of the jet breakup location, which was calculated to be slightly further downstream than experimentally measured. In any case, the discrepancy between the simulated and experimental results is small.

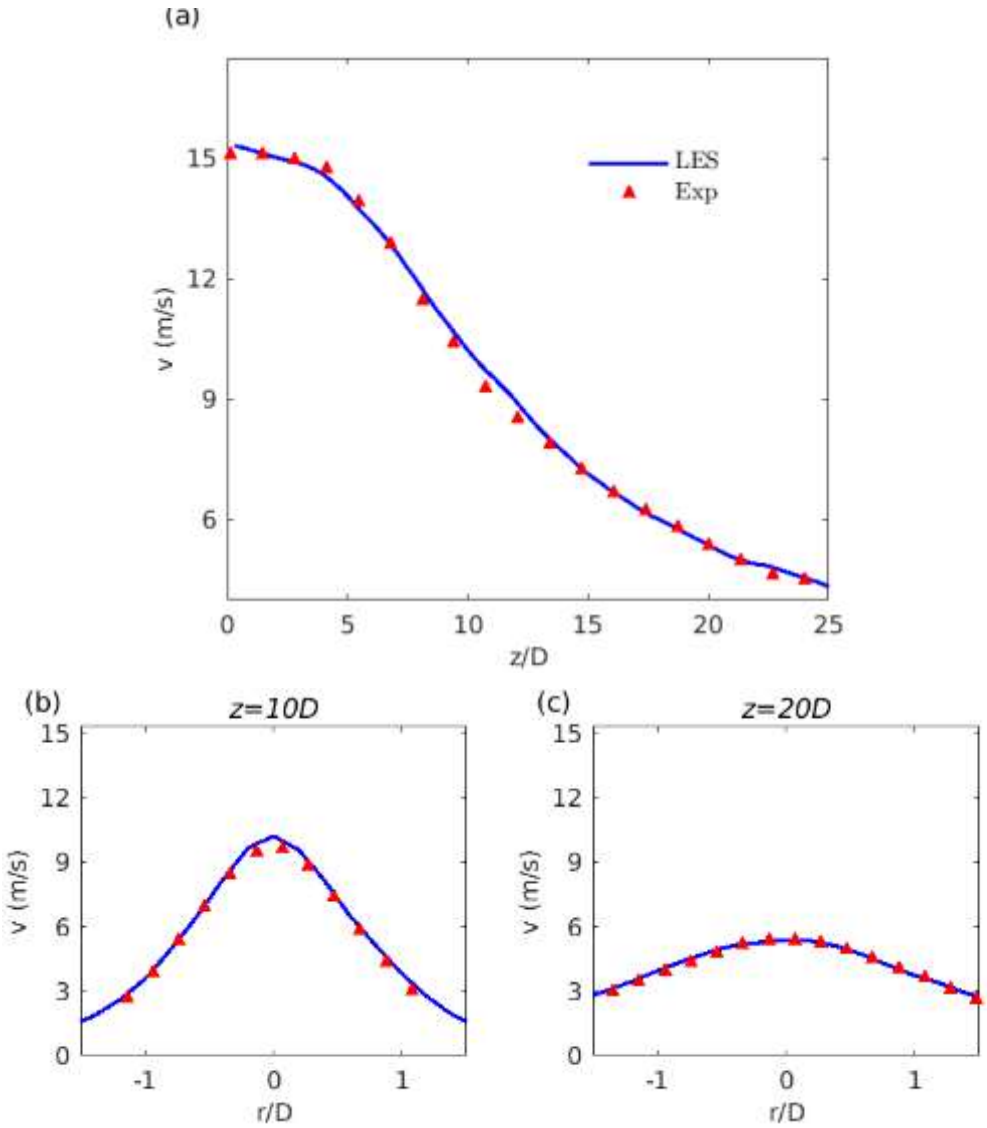


Figure 6 The mean axial velocity profiles of the carrier phase for a single-phase jet (a) along the centreline and along two radial extents at (b) $z/D = 10$ and (c) $z/D = 20$. The experimental data is given by Lau & Nathan (2016).

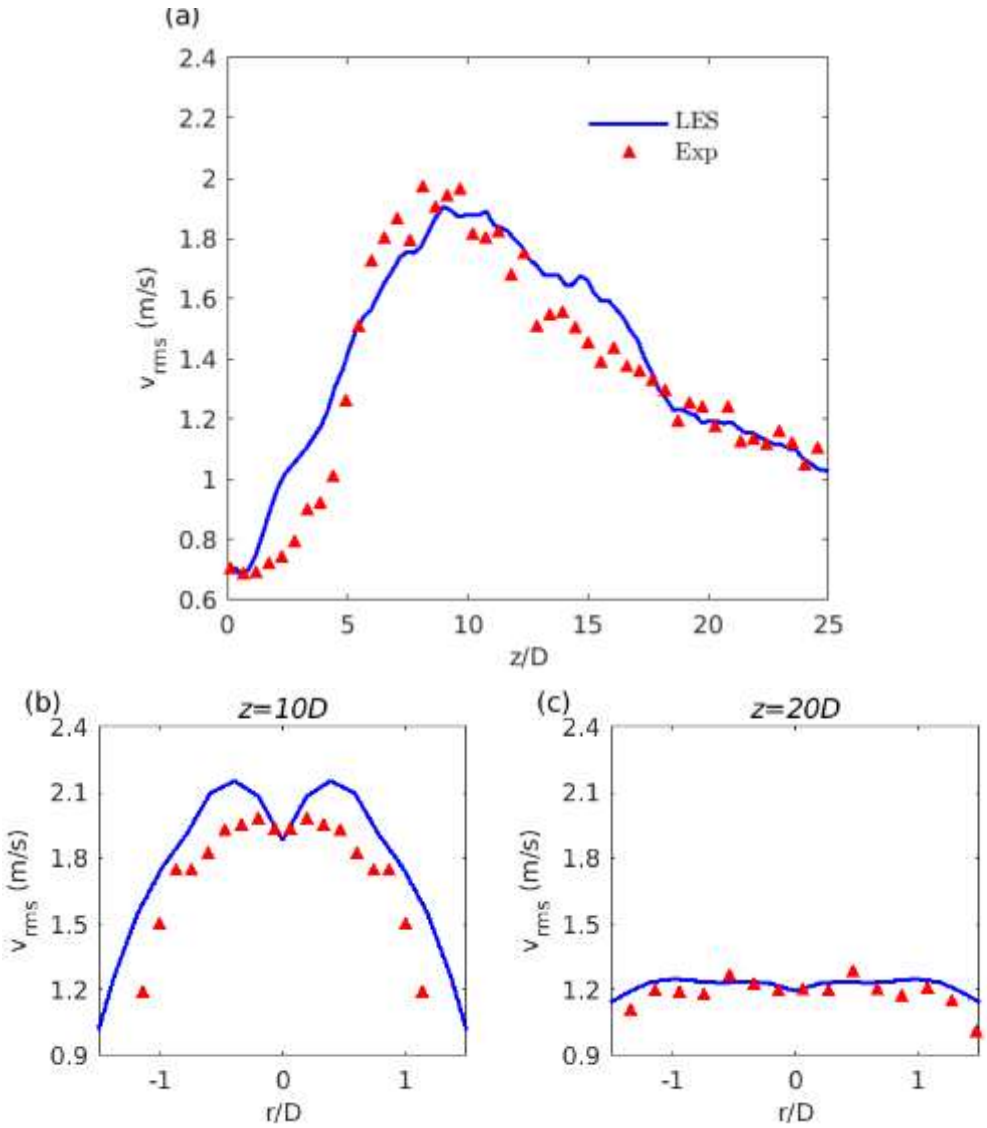


Figure 7 The axial velocity RMS of the carrier phase for a single-phase jet (a) along the centreline and along two radial extents at (b) $z/D = 10$ and (c) $z/D = 20$. The experimental data are given by Lau & Nathan (2016).

3.2. Polydisperse jet

The validation of the PDF-PBE model against the measured data is presented in the first part of this section. This is followed by a detailed analysis of the effects of particle size on their dispersion and volume fraction in a two-way coupling regime.

3.2.1 Validation

Figure 8 presents the time-averaged particle axial velocity (averaged across all particle sizes) along the centreline together with the radial profiles of particle axial velocity at $z/D = 10$ and 20 for both the experimental measurements and the PDF-PBE model. There is an excellent agreement between the PDF-PBE model and the experimental data for the mean particle velocity along the centreline although the predicted values are slightly higher by 3.1% than the measured values at $z/D = 0$ near the inlet (Figure 9a). This could be due to the inlet boundary condition that assigns patch (carrier gas) velocities to the injected particles at the inlet. It is expected that a more sophisticated method, such as utilising a pre-process particle-laden pipe simulation would improve the agreement at the inlet.

The agreement between the PDF-PBE and experimental data is very good for the radial profiles, particularly towards the centreline while the maximum difference occurs near the edge of the jet, i.e. at $|r/D| = 1$. The reason for this difference is because the PDF-PBE model slightly overpredicts the expansion of the jet, leading to greater values of particle velocity towards the extremities.

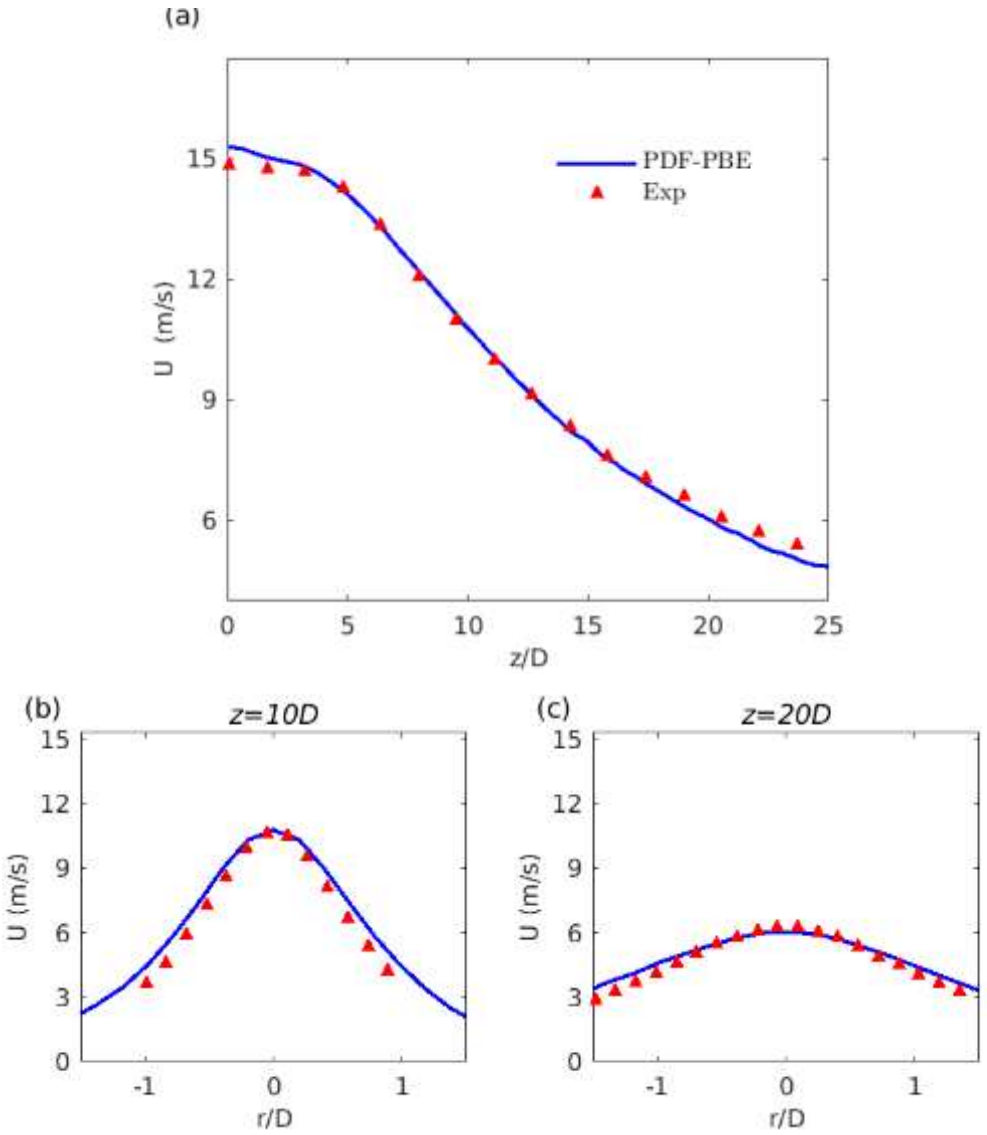


Figure 8 Polydisperse jet: centreline and radial profiles of mean particle velocity.

Figure 9 presents the centreline and radial profiles of the particle axial velocity RMS. Overall, a satisfactory agreement is achieved. It can be seen that the predicted particle velocity RMS initially follows the measurements data, however, it is underpredicted at the axial locations $5 < z/D < 12$, with the agreement improving further downstream. The peak RMS velocity is underpredicted and its location is further downstream compared to the measurements. As shown in Figure 7a, there is a slight discrepancy between the LES of the carrier phase and measurements that may partly contribute to the underprediction of particle RMS by the simulations. Furthermore, the subgrid model used to construct the carrier phase velocity fluctuations at the particle location may also contribute to the observed discrepancy. Here, we use the subgrid model developed by Pozorski & Apte (2009) that neglects the gradient of the turbulent stress, as well as the gradient of the filtered velocity (Innocenti et al., 2016).

These simplifications may, in particular, cause errors in predicting the velocity of particles that are more responsive to the turbulence (i.e., particles with lower Stokes numbers). Additionally, it is also plausible that the experimental results overpredict the peak particle velocity RMS values. During the processing of the experimental data, a single velocity value within an interrogation window of finite size is obtained for any given location and timestep. However, in a polydisperse flow, a range of particle sizes, each with potentially different velocities, may be captured in each interrogation window. Because the particle size distribution in any given interrogation window may vary between timesteps, which may result in a measured value of particle velocity RMS that is greater than the true value.

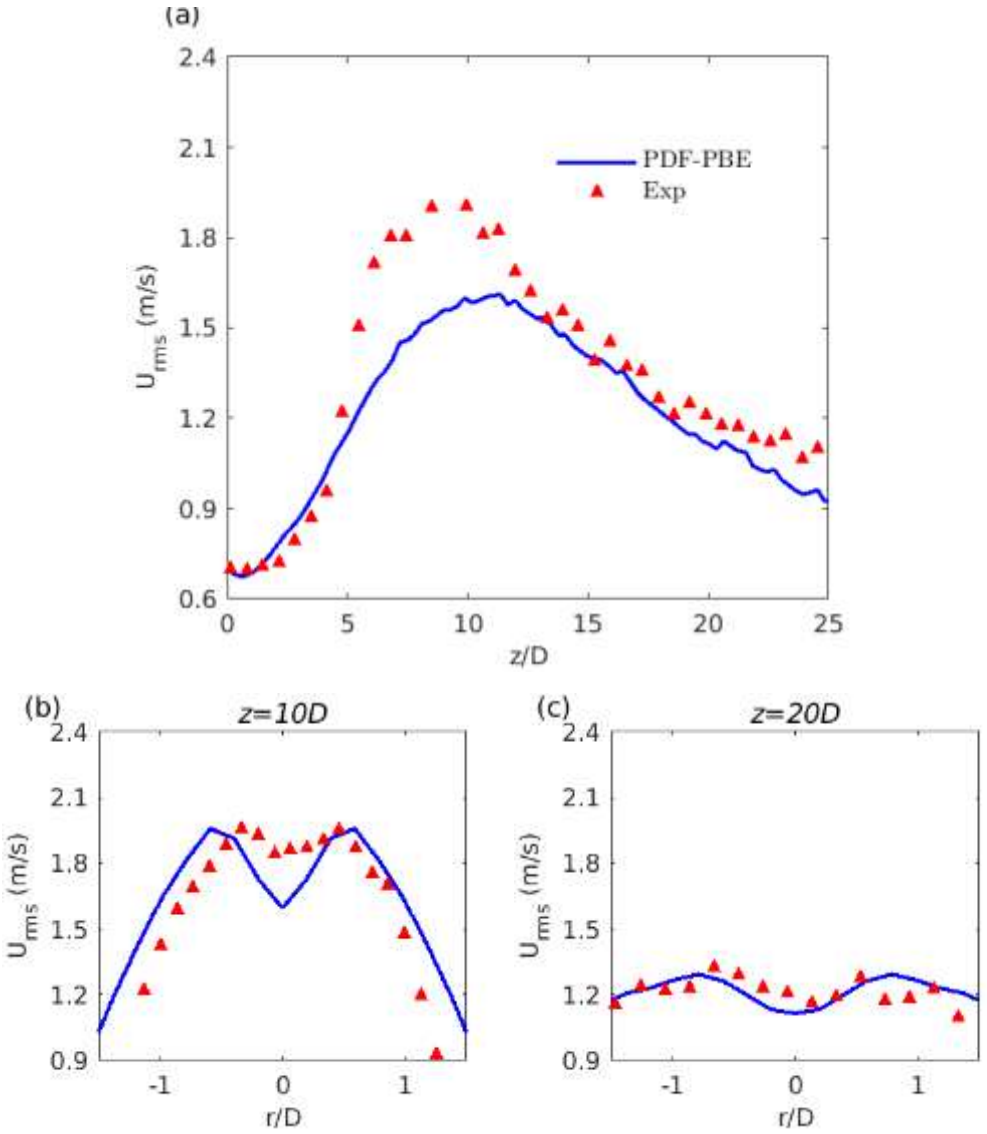


Figure 9 Polydisperse jet: centreline and radial profiles of axial particle velocity RMS.

The comparison between the simulations and measurements for the mean intensity (pseudo particle volume fraction) is shown in Figure 10 where the values are normalised by the value at the inlet. The results show that the PDF-PBE model does capture the pseudo volume fraction hump although its location is slightly upstream of the current experimental data with polydispersed particles. In the near field, $z/D < 6$, the agreement between the PDF-PBE model and the measurements is satisfactory

while the model result decays more rapidly and underpredicts the measured pseudo volume fraction further downstream. The observed discrepancy between the experimental and modelled results may be partially due to the sensitivity of these profiles to the spatial distribution of particle sizes within the flow, as is discussed in the next sub-section.

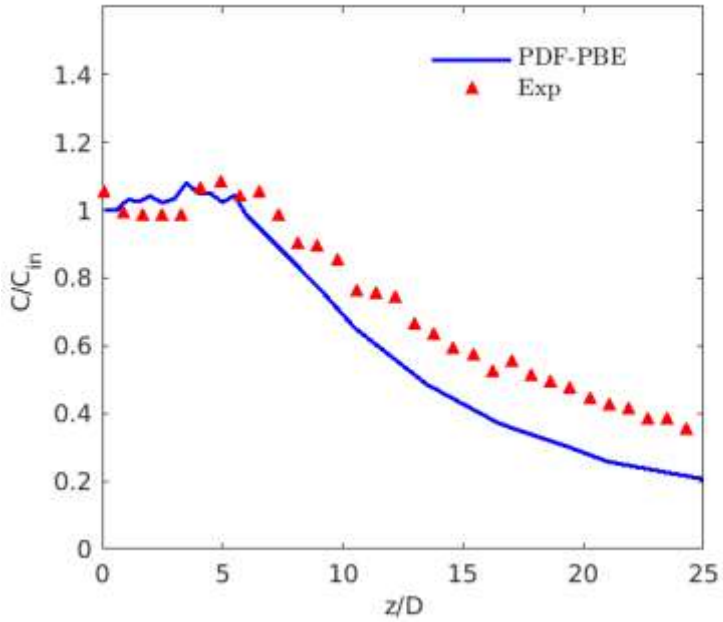


Figure 10 Polydisperse jet: normalised mean intensity (pseudo volume fraction) along the centreline.

3.2.2 Effect of inlet Stokes number

To shed further light on the particle dynamics, the particle velocity and particle volume fraction conditioned by particle size are presented in Figure 11-Figure 14. Note that such measurements for each particle size are not possible with the current experimental setup and hence only the PDF-PBE results are discussed here. The results are presented for particles with different St_{in} ranging from 0.03 to 25.

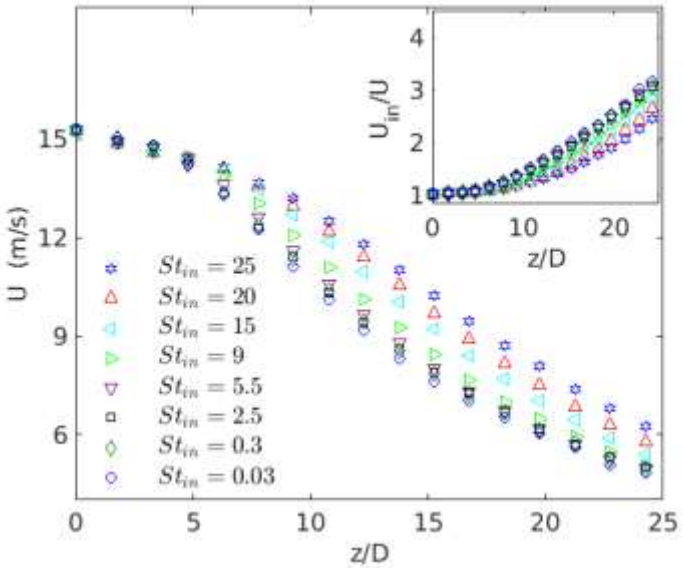


Figure 11 Polydisperse jet: Modelled mean particle axial velocity conditioned by particle size along the centreline. The inset shows the inverse axial (normalised) velocity, defined as U_{in}/U.

Figure 11, showing the predicted mean axial particle velocity along the centreline, reveals that the particles with greater St_{in} have lower axial decay rate since they are less affected by the carrier phase flow whereas the particles with lower St_{in} are slowed down by the carrier phase flow and have a higher axial decay rate. This trend is consistent with the previous observations of both monodispersed (Lau & Nathan, 2016) and polydispersed experimental data (Prevost et al., 1996). At all axial locations, the particle axial velocities decrease as their Stokes number decreases. The inverse axial (normalised) velocity, defined as U_{in}/U where the subscript "*in*" refers to the value at the inlet, is also shown as an inset in Figure 11. It demonstrates that at the far-field, the trend is linear, confirming the flow approaches the self-similarity in the velocity profiles. It can be seen that in the near field ($z/D < 5$) there is a similar velocity decay rate for all sizes, while further downstream the decay rate varies as particle inlet Stokes number increases.

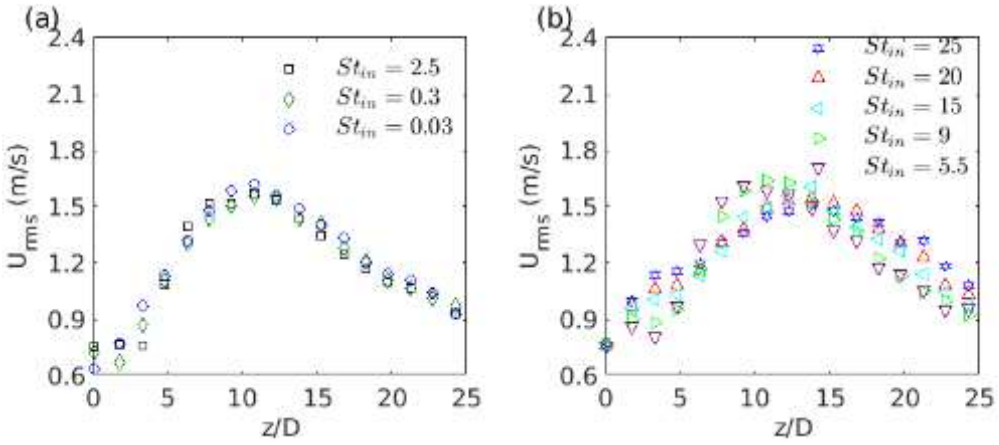


Figure 12 Polydisperse jet: Modelled particle axial velocity RMS conditioned by particle size along the centreline.

The centreline profiles of predicted particle axial velocity RMS are presented in Figure 12. As can be seen, in the near field, $z/D < 5$, the RMS particle velocities are significantly different for different particle sizes, despite their mean velocities being approximately the same in the near field region. Most particles with $St_{in} < 9$ (except particles with $St_{in} = 5.5$) see a peak RMS value at around $z/D = 10$ as can be seen from Figure 12 (a), while for most particles with $St_{in} > 15$, the peak value shifted downstream to about $z/D = 13.2$ 10 (Figure 12 b), because the larger particles are less responsive to the carrier phase, which in turn leads to a longer uninterrupted core flow.

Figure 13 shows the radial profiles of mean particle axial velocity and its RMS for different particle sizes at $z/D = 10$ and 20. As the particle size (or their St_{in}) decreases, the mean particle axial velocity decreases throughout the radial extent of the jet, confirming the radial dispersion of larger particles is less than the particles with lower inlet Stokes numbers since they are less responsive to the carrier phase. At $z/D = 10$, the particle RMS velocities show a similar trend for all particle sizes, with a local minimum on the axis and a peak at the shear layer $|x/D| \sim 0.8$, as expected. Further downstream, at $z/D = 20$, particles with greater St_{in} typically have higher RMS velocities, because the inertial particles retain high values of the RMS for greater downstream distances, as previously discussed.

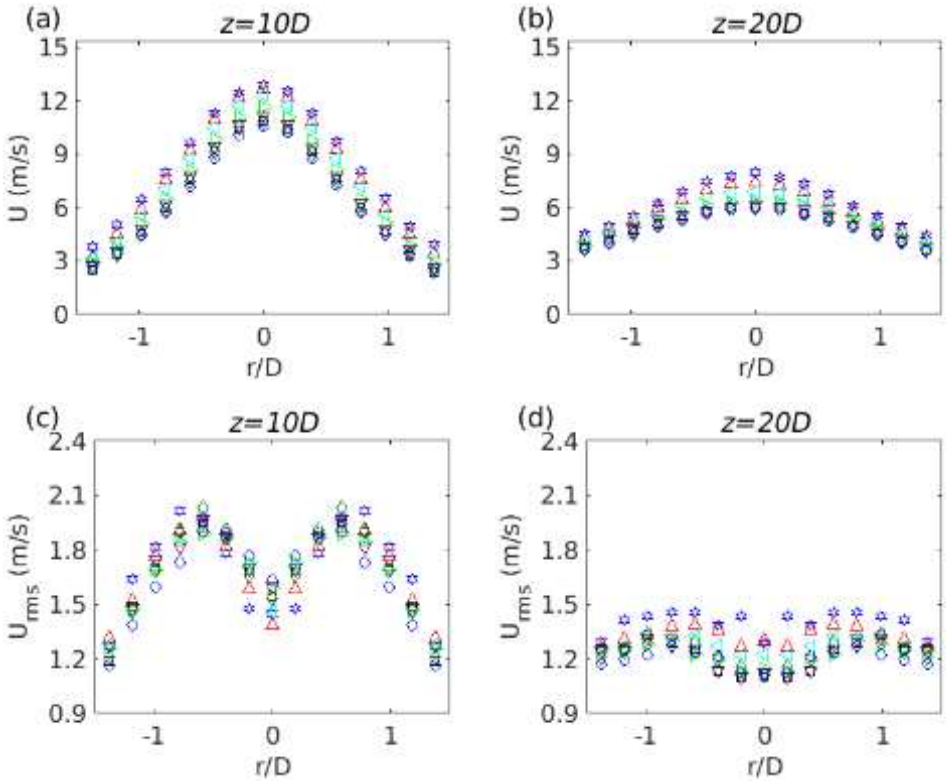


Figure 13 Polydisperse jet: Radial profiles of modelled mean particle axial velocity and its RMS conditioned by the particle size. The legend is the same as Figure 14.

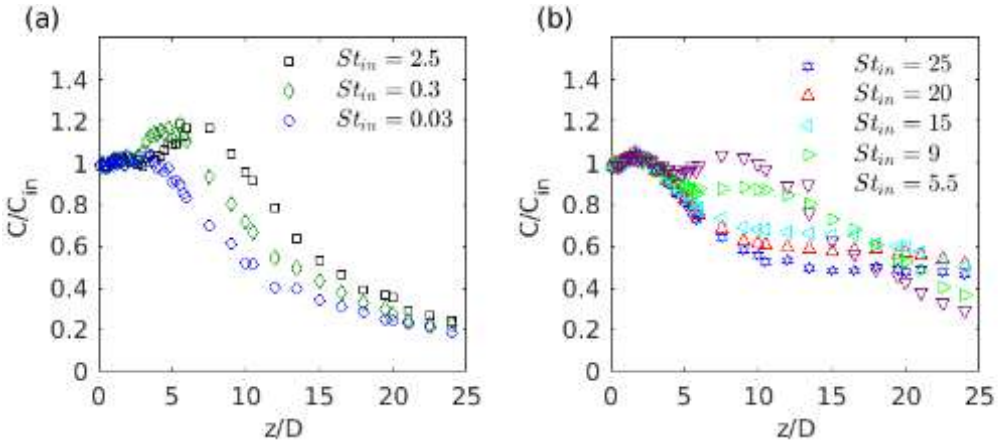


Figure 14 Polydisperse jet: Normalised modelled mean intensity (pseudo volume fraction) along the centreline conditioned by the particle size.

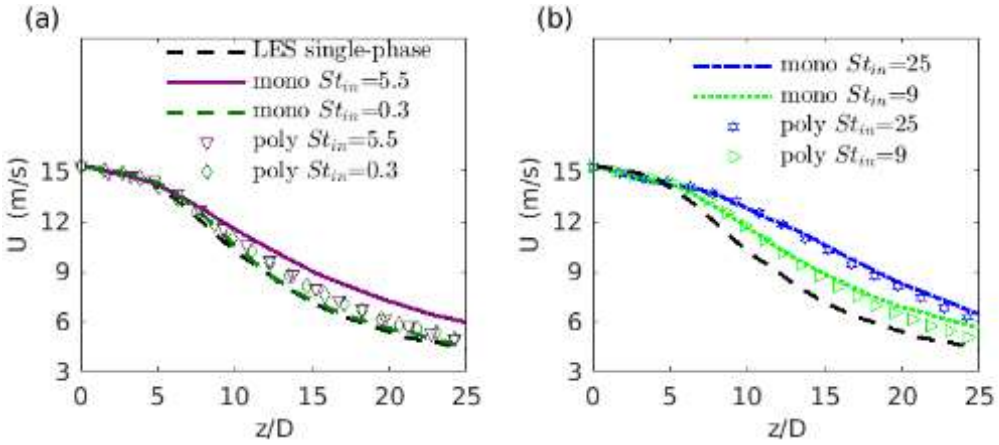
Figure 14 presents the normalised intensity, which is a measure of the particle pseudo volume fraction, conditioned on particle size along the centreline. The results are presented as two separate sub-figures for clarity. The centreline volume fraction profile is strongly influenced by the Stokes number. This is an important finding because it shows that in a polydisperse particle-laden jet, the volume fraction distributions of different particle sizes within the same jet may be significantly different both to the volume fractions of other size classes and the average across all sizes. The results reveal that the centreline particle volume fraction is approximately constant for the first ~ 2-3 diameters downstream from the exit. Further downstream, for $0.3 < St_{in} < 9$, the volume fraction profiles show a local

maximum, with the location of the local maximum moving downstream with increasing St_{in}. Interestingly, these trends are consistent with previous measurements of monodisperse jets, although the absolute values may differ (Lau & Nathan, 2016; Picano et al., 2010). As postulated by Lau & Nathan (2016), in monodispersed cases with $St_{in} < 3$, the cause of the hump is a combination of particle axial deceleration and the radial migration. On the other hand, for monodispersed cases with greater St_{in}, the peak volume fraction disappears and the volume fraction continuously decreases along the centreline. The results show that even in a polydisperse jet, particles of different size classes may concentrate at different axial locations, such that their time-averaged number density forms local maxima at different axial locations. In the far-field ($z/D > 15$) the volume fraction profiles of particles with $St_{in} \leq 15$ continue to decrease monotonically, with lower Stokes number particles showing a greater decay rate in centreline volume fraction, as expected. However, for the two higher St_{in} cases, St_{in} = 20 and 25, the decay rate in the range $5 < z/D < 10$ appears to be significantly different to that for $z/D > 10$, suggesting there may be two regimes which are characterised by significantly different volume fraction decay rates. Interestingly there are no local maxima in particle volume fraction for $St_{in} = 0.03$ since these particles closely follow the carrier phase.

The results presented in Figure 15a may also provide an explanation for the discrepancy in the average centreline profiles of pseudo-concentration profiles for all Stokes numbers (i.e. all particle diameters) between the simulated and experimental results (also presented in Figure 11). The profiles in Figure 15a show that the average experimental measurements tend more towards the profiles of the larger Stokes numbers than do the average simulated results. The bias in the experimentally measured pseudo-concentration towards larger particle sizes is attributed to the limited dynamic range of the cameras, which results in some loss in signal from the smaller particles, which generate weaker signal, so that some is indistinguishable from the noise.

3.3. Polydisperse versus monodisperse jets

To further understand the effects of the polydispersion on a particle-laden two-way coupled flow, a comparison is made between the polydisperse two-way coupled and monodisperse two-way coupled jets in this section. The list of monodisperse simulations is given in Table 2.



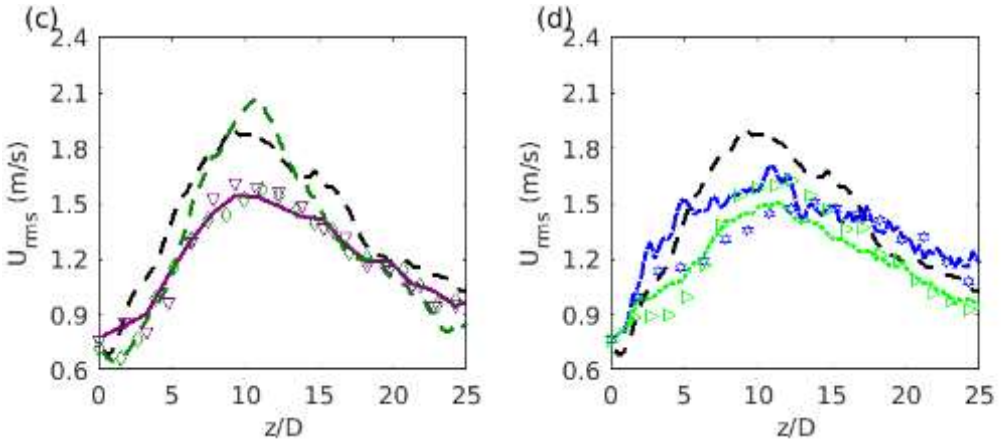


Figure 15 Polydisperse jet versus monodisperse jet: Modelled mean particle axial velocity and its RMS along the centreline.

Figure 15 - Figure 17 present the simulated mean and RMS particle velocities for four inlet Stokes numbers, St_{in} = 0.3, 5.5, 9 and 25, for both the polydisperse (open symbols) and monodisperse (solid lines) cases. The single-phase LES results are also presented in these figures by dashed black lines. To improve clarity, the results of particles with $St_{in} = 0.3$ and 5.5 are illustrated in the left subfigures (a) and (c) while the results of particles with $St_{in} = 9$ and 25 are shown in the right subfigures (b) and (d). Several observations can be made here.

Generally, in both monodisperse (solid lines) and polydisperse (open symbols) cases, the larger particles exceed the gas-phase velocity in the far-field due to their inertia. The mean and RMS velocities of the monodispersed particles with $St_{in} = 0.3$ approach those of the single-phase on the centreline (Figure 15a). This is expected as the Stokes numbers are sufficiently small such that the particles closely follow the gas-phase. However, the mean and RMS velocities for the polydispersed case at the same Stokes number, $St_{in} = 0.3$, is significantly different from those of both the single-phase and the monodispersed case. This is because the larger particles in the polydispersed case significantly influence the gas-phase (consistent with the flow being in the two-way coupled regime), which in turn impacts the size-averaged velocity distributions in the jet. For particles with $St_{in} = 5.5$, an opposite trend is observed (Figure 15a). This is because in the polydispersed case, the small particles which follow the flow effectively increase the inertia of the fluid phase. The polydisperse particles show a greater decay rate than the monodisperse particles at the same Stokes number, due to the influence of the small particles on the gas-phase in the polydisperse case.

The difference in the RMS velocity profiles between $St_{in} = 0.3$ and 5.5 (Figure 15c) is more prominent in the monodisperse case than in the polydisperse case which could be due to the accelerating/decelerating effects of particles on the carrier flow. It may conclude that there is a significant particle momentum transfer between the two phases and/or significant large-scale mixing within the gas-phase.

For larger particles with St_{in} of 9 and 25, particles in the polydisperse jet have higher axial decay rates than in the monodisperse jet (Figure 15b). As shown in Figure 15b, particles with $St_{in} = 25$ in the polydisperse jet initially shows a higher axial decay rate than particles with $St_{in} = 9$. For $6.3 < z/D < 14.7$, the larger particles have a lower axial decay rate, shifting the peak velocity RMS further downstream for particles with $St_{in} = 25$. On the other hand, in the monodisperse jets, both $St_{in} = 9$

and 25 show a similar trend where the peak RMS occurs at $z/D = 11.3$. For particles with $St_{in} = 25$, compared to the single-phase turbulence intensities, the particle RMS velocities are lower for $z/D < 17$. This is attributed to modulation of the gas-phase turbulence by the particles, together with the inertia of the particles, which causes them to only partially respond to the velocity fluctuations in the gas phase. Further downstream, the inertia of the particles also ensures that the particles retain their velocity fluctuations and hence the values of particle RMS velocities for the large Stokes number particles (St_{in}=25) exceed that of the single-phase.

The results show that the radial profiles of mean particle velocity between the monodispersed and polydispersed cases are similar at both $z/D = 10$ and 20 for all four investigated Stokes numbers. However, the RMS particle velocities between the monodispersed case are significantly different from that of the polydisperse case, for all Stokes numbers at $z/D = 10$ (Figure 16c and Figure 16d). For $St_{in} = 5.5$, the particle velocity RMS is higher in the polydisperse jet than in the monodisperse jet. This is expected because the larger distribution of particle sizes in the polydispersed case results in a larger range of instantaneous particle velocities, which in turn leads to greater values of velocity RMS. Further downstream at $z/D = 20$, the monodisperse case shows a flatter RMS velocity profile for both St_{in} of 0.3 and 5.5 (Figure 17c) whereas the differences between polydisperse and monodisperse cases for both St_{in} of 9 and 25 are marginal (Figure 17d).

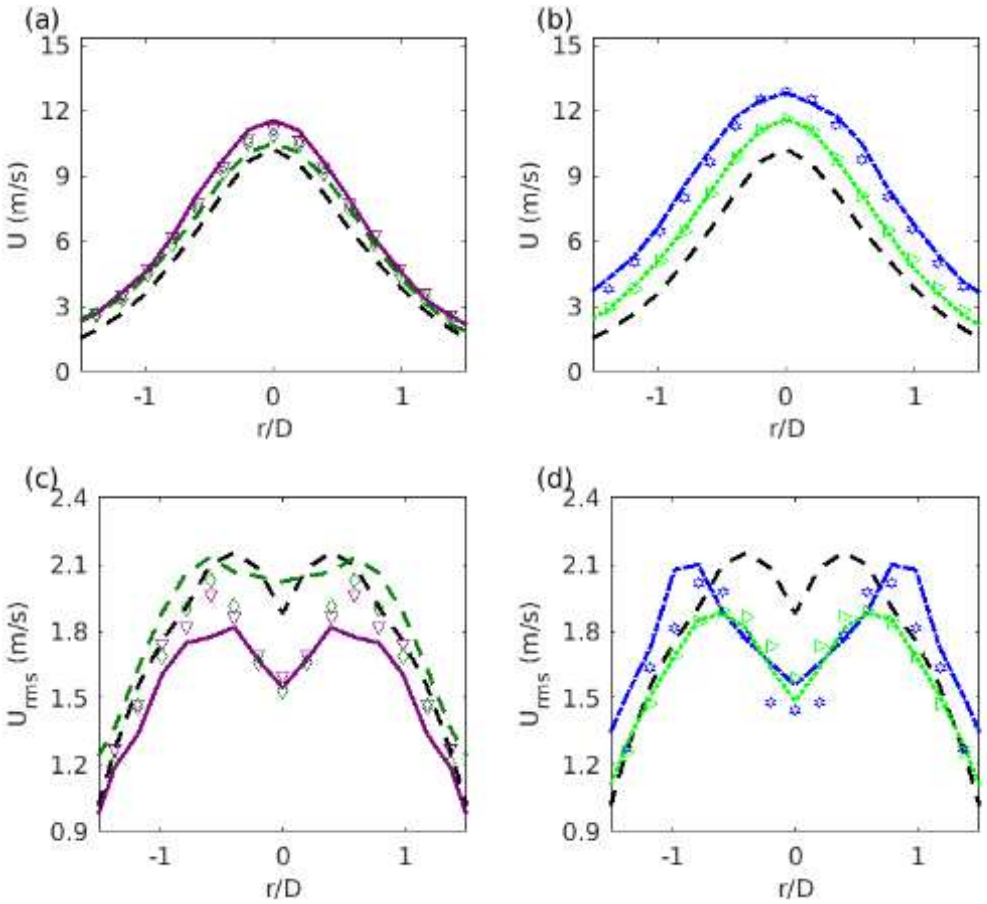


Figure 16 Polydisperse jet versus monodisperse jet: Radial profiles of modelled mean particle axial velocity and its RMS at $z/D = 10$. The legend is the same as Figure 13.

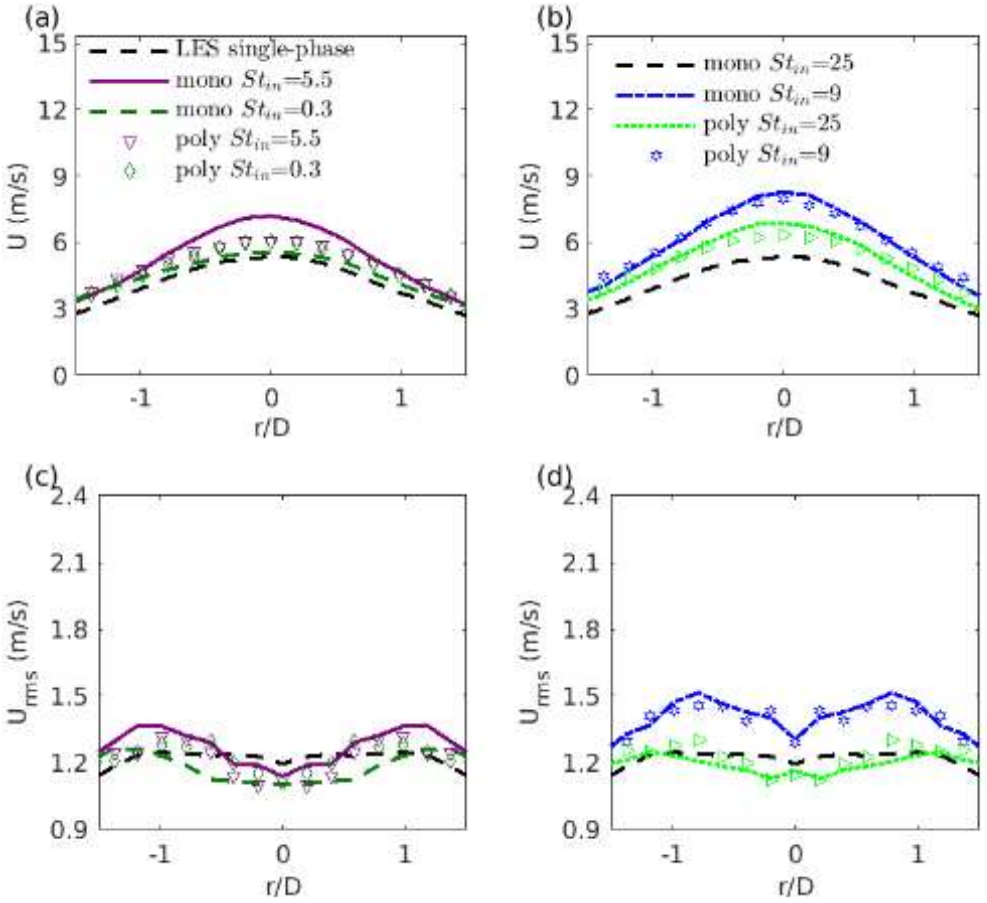


Figure 17 Polydisperse jet versus monodisperse jet: Radial profiles of modelled mean particle axial velocity and its RMS at $z/D = 20$.

Figure 18 compares the RMS radial velocity of particles, $U_{r,rms}$ between the polydisperse and monodisperse jets. For all sizes, the RMS velocity initially decreases just downstream from the exit plane. Further downstream, $U_{r,rms}$ for the smallest particles ($St = 0.3$) increases up to a maximum value, which occurs approximately at $z/D = 10.4$. This location is slightly downstream from the corresponding location for the single-phase data, $z/D = 8.1$, consistent with the particles having greater inertia than the gas-phase. For larger particles ($St_{in} = 9$ and 25), $U_{r,rms}$ decreases with axial distance for $0 < z/D < 5$, before approaching a relatively constant value that is approximately the same for both the monodispersed and polydispersed cases at the same Stokes number. The difference between the monodisperse and polydisperse case is most prominent for $St_{in} = 5.5$. This is consistent with the previous experimental data of (Lau & Nathan, 2016), which showed that the largest difference for a monodisperse particle-laden jet occurs within the range $1.4 < St_{in} \leq 5.6$.

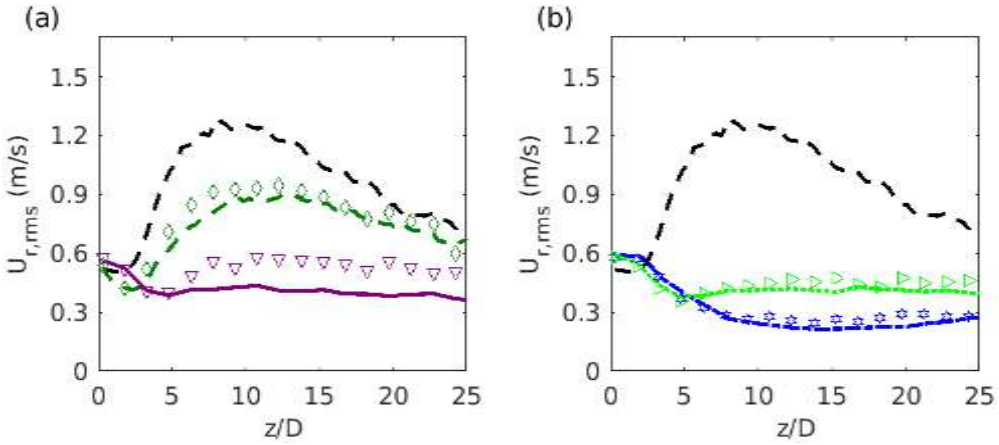


Figure 18 Polydisperse jet versus monodisperse jet: Modelled particle radial velocity RMS along the centreline. The legend is the same as Figure 17.

The normalised pseudo volume fraction presented in Figure 19 shows that the monodisperse and polydisperse profiles follow the same trends for the same inlet Stokes numbers. In both jets, for the smallest particles, there is a clear hump where the volume fraction reaches its highest value at $z/D = 5$. For $St_{in} = 0.3$ and 5.5, there is a greater axial volume fraction decay rate downstream of the humps in the polydispersed case relative to the monodispersed case, however, the converse is true for larger particles with $St_{in} = 9$ and 25. For cases where there are local maxima, the centreline volume fraction decays approximately linearly with the axial distance downstream from the local maxima.

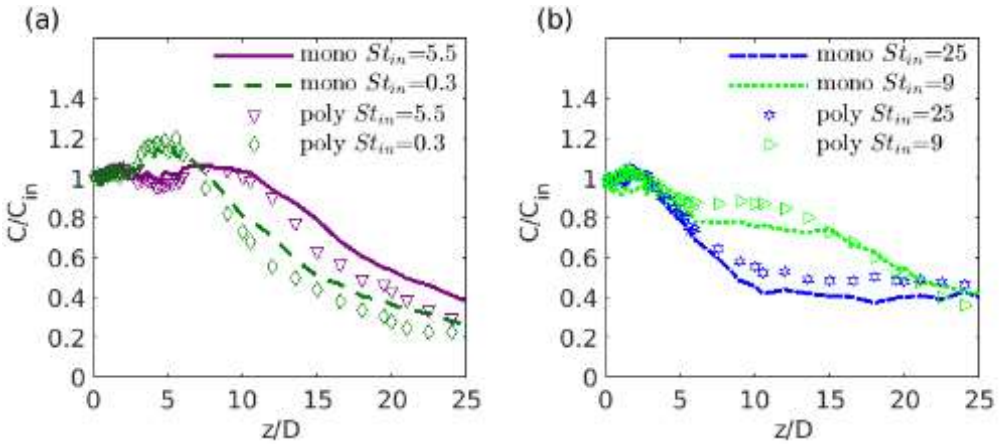


Figure 19 Polydisperse jet versus monodisperse jet: Normalised modelled mean intensity (pseudo volume fraction) along the centreline. The legend is the same as Figure 13.

For an axisymmetric turbulent jet, it is well established that the mean centreline velocity and scalar quantities decrease linearly with axial distance (Townsend, 1976) in the far-field. The decay coefficient in far-felid can be written as (Sautet & Stepowski, 1995);

$$K_{1,\beta} = \frac{\beta}{\beta_{in}} * \frac{\sqrt{1-\lambda^{-1}} * \left(z - z_{01,\beta}\right)}{d_{\epsilon}} \tag{14}$$

where β is the mean velocity (U) or mean (pseudo) volume fraction (intensity) (C) along the centreline, $z_{01,\beta}$ is the virtual origin based on the decay, d_{ϵ} is the equivalent diameter, and $\sqrt{1-\lambda^{-1}}$

is a correction term where λ is the jet-to-co-flow velocity ratio (Lau & Nathan, 2016). The commonly accepted form of the equivalent diameter is written as (Mi et al., 2001; Papadopoulos & Pitts, 1998);

$$d_\epsilon = \frac{2M_{in}}{(\pi\rho J_{in})^{0.5}} \tag{15}$$

where M_{in} and J_{in} are the mass and momentum flux of the jet at the inlet. The values of M_{in}, J_{in} and d_ϵ are adopted from (Lau & Nathan, 2016) that used the same experimental set-up.

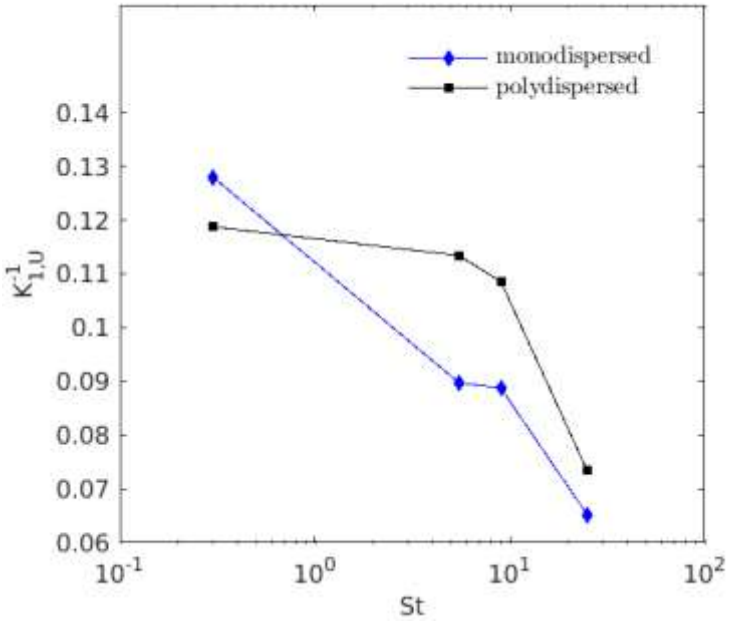


Figure 20 Polydisperse jet versus monodisperse jet: The decay coefficient, (a) $K_{1,U}^{-1}$, for modelled mean particle velocity evaluated based on data for z/D > 15

Figure 20 presents the dependence of the inverse velocity decay coefficient $K_{1,U}^{-1}$ in the far-field ($z/D > 15$) where U_{in}/U shows a linear trend for both the monodisperse and the polydisperse simulations. The maximum value of 0.13 is consistent with the value of $K_{1,U}^{-1} = 0.166$ for the modelled single-phase jet, not shown here, which is also consistent with the previously measured value of 0.164 (Lau & Nathan, 2016). An increase in the Stokes number leads to a decrease in the value of $K_{1,U}^{-1}$, indicating that smaller particles follow the flow more closely and hence radially disperse more compared to larger particles, as expected. For both monodisperse and polydisperse jets, the jet decay coefficient for the two-phase jet is lower than the single-phase jet suggesting that the presence of particles significantly reduces the jet decay rate. It is also worth noting that the values of $K_{1,U}^{-1}$ in the present model for the monodisperse particles matches the previous experimental results (Lau & Nathan, 2016) to within less than 10% for all investigated Stokes numbers, providing further evidence of the accuracy of the simulations.

While the velocity decay rates for the monodisperse jet decreases significantly with an increase in the Stokes number, the decay rates for the polydisperse case only show a slight decrease between $0.35 \leq St_{in} \leq 11.2$. This is attributed to the momentum coupling between the particles (of all sizes) and the fluid phase in the polydisperse case. More specifically, the fluid phase velocity is expected to be modified (non-linearly) by the velocity field of *all* particle sizes. The fluid phase, in turn, is expected to modify the particle phase for all Stokes numbers. That is, the velocity decay rates of the larger

particles is expected to more closely approach that of small particles, and vice versa. This results in a weaker effect of Stokes numbers on the polydisperse velocity field. For very large Stokes number particles, $St_{in} \geq 22.4$, this two-way coupling effect is not as pronounced because the particles are sufficiently large to be less influenced by the "modified" fluid phase. Taken together, it can be inferred that the effect of polydispersity is to decrease the velocity decay rates for low Stokes number particles (due to the influence of large particles) and increase the velocity decay for high Stokes number particles (due to the influence of small particles) relative to the monodisperse case.

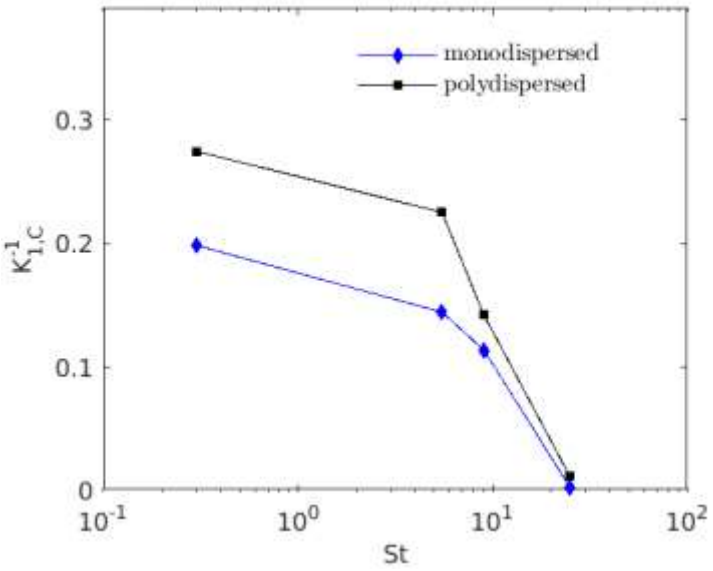


Figure 21 Polydisperse jet versus monodisperse jet: The decay coefficient $K_{1,C}^{-1}$ for modelled mean particle volume fraction evaluated based on data for z/D > 15

Figure 21 presents the dependence of the inverse volume fraction decay coefficient, $K_{1,C}^{-1}$ in the far-field. $K_{1,C}^{-1}$ decreases with increasing the Stokes number in both monodisperse and polydisperse simulations. The values of $K_{1,C}^{-1}$ are higher for the polydisperse case for the smaller St_{in} while the difference between the monodisperse and polydisperse data becomes marginal at the larger St_{in} which is consistent with the findings in Figure 19.

4. Conclusion

Experimental and computational modelling studies were conducted for a polydisperse jet with the inlet Reynolds number of 10,000 and the inlet Stokes number, St_{in}, ranging from 0.03 to 25. The evolution of particle velocity and volume fraction was measured using digital particle image velocimetry and planar nephelometry (PIV-PN) simultaneously. The simulations were conducted using a two-way large eddy simulation (LES) coupled with a probability density function of the population balance equation (PDF-PBE) model which has been recently developed by Salehi et al. (2017). There is sufficient agreement between the measurements and the simulation results for both carrier phase and particles to have confidence in the trends, despite some differences in the absolute values.

This study showed that in a polydisperse jet, the smaller particles with lower St_{in} have a higher decay rate while the larger particles with greater St_{in} have a lower axial decay rate. This deduction implied that the particles with lower Stokes numbers were slowed down by the carrier phase flow while the

particles with higher Stokes numbers were less affected by the carrier phase flow. This is consistent with previous works for monodisperse jets. The polydisperse results confirmed that volume fraction distributions of different particle sizes within the same jet were significantly different to the volume fractions of other size classes. There were local maxima in particle volume fraction along the centreline for all particle sizes except particles with $St_{in} = 0.03$ since they closely follow the carrier phase. The hump occurred at different axial locations for different particle sizes which were due to particle deceleration and radial migration.

The simulations for a series of monodisperse jets were conducted to shed light on the effect of polydispersity. It was found that small monodispersed particle ($St_{in} = 0.3$) approached the single-phase velocity on the centreline however for the polydisperse jet, at the same Stokes number, the particle axial velocity was larger than single-phase velocity. This is because of the effect of larger particles on the gas phase that in turn impacts smaller particles in the polydisperse jet. For larger particles ($St_{in} > 0.3$), the trend was opposite since in the polydispersed case, the small particles effectively increase the inertia of the fluid phase. For particles with very large St_{in}, the differences between particle axial velocity in monodisperse and polydisperse jets became marginal. In general, the particle radial velocity RMS were lower than the single-phase turbulence intensities in both monodisperse and polydisperse cases due to the partial response of the particles to turbulent motions in the gas phase, together with a possible role of turbulence modulation of the gas phase. All the investigated monodispersed particles showed lower radial velocity RMS compared to the polydisperse jet, at the same Stokes number, along the centreline although the difference was only significant for particles with $St_{in} = 5.5$.

The concentration of particles was different in monodisperse and polydisperse jets due to the impact of particles on the carrier phase that in turn affects particles' axial and radial velocity and hence their volume fraction. The volume fraction of particles with $St_{in} = 0.3$ in the polydisperse jet was less than the monodisperse jet, at the same Stokes number, along the centreline due to the impact of larger particles. A similar trend was observed for particles with $St_{in} = 5.5$ even though the decay rate for their axial velocity was lower in the polydisperse case. In the polydisperse case, these particles showed significantly higher radial velocity RMS than the monodispersed particles with $St_{in} = 5.5$, demonstrating they were more pushed away from the centreline and hence their volume fraction became lower than monodispersed particles with $St_{in} = 5.5$. For larger particles ($St_{in} = 9$ and 25), an opposite trend was observed since, in the polydisperse jet, they were more slowed down by the carrier phase compare to the monodisperse jet at the same Stokes number, and hence their volume fraction was higher along the centreline.

Acknowledgement

The authors acknowledge the AWS service funded by Macquarie University for providing computing resources.

Reference

Aísa, L., Garcia, J. A., Cerecedo, L. M., García Palacín, I., & Calvo, E. (2002). Particle concentration and local mass flux measurements in two-phase flows with PDA. Applications to a study on the dispersion of spherical particles in a turbulent air jet. *International Journal of Multiphase Flow*, *28*(2), 301–324. https://doi.org/10.1016/S0301-9322(01)00071-4

Alletto, M., & Breuer, M. (2012). One-way, two-way and four-way coupled LES predictions of a particle-laden turbulent flow at high mass loading downstream of a confined bluff body. *International Journal of Multiphase Flow*, *45*, 70–90. https://doi.org/10.1016/j.ijmultiphaseflow.2012.05.005

Almeida, T. G., & Jaberi, F. A. (2008). Large-eddy simulation of a dispersed particle-laden turbulent round jet. *International Journal of Heat and Mass Transfer*, *51*(3–4), 683–695. https://doi.org/10.1016/j.ijheatmasstransfer.2007.04.023

Apte, S. V., Mahesh, K., Moin, P., & Oefelein, J. C. (2003). Large-eddy simulation of swirling particle-laden flows in a coaxial-jet combustor. *International Journal of Multiphase Flow*, *29*(8), 1311–1331. https://doi.org/10.1016/S0301-9322(03)00104-6

Balachandar, S., & Eaton, J. K. (2010). Turbulent dispersed multiphase flow. *Annual Review of Fluid Mechanics*, *42*, 111–133. https://doi.org/10.1146/annurev.fluid.010908.165243

Barve, A. V., Sahu, S., & Anupindi, K. (2020). Effect of co-flow velocity ratio on evolution of poly-disperse particles in coaxial turbulent jets: A large-eddy simulation study. *Physics of Fluids*, *32*(9), 093303. https://doi.org/10.1063/5.0017663

Berrouk, A. S., Laurence, D., Riley, J. J., & Stock, D. E. (2007). Stochastic modelling of inertial particle dispersion by subgrid motion for LES of high Reynolds number pipe flow. *Journal of Turbulence*, *8*, 1–20. https://doi.org/10.1080/14685240701615952

Bogusławski, L., & Popiel, C. O. (1979). Flow structure of the free round turbulent jet in the initial region. *Journal of Fluid Mechanics*, *90*(3), 531–539. https://doi.org/10.1017/S0022112079002378

Boree, J., Ishima, T., & Flour, I. (2001). The effect of mass loading and inter-particle collisions on the development of the polydispersed two-phase flow downstream of a confined bluff body. *Journal of Fluid Mechanics*, *443*, 129–165. https://doi.org/10.1017/S0022112001005134

Chen, H., Chen, Y., Hsieh, H. T., & Siegel, N. (2007). Computational fluid dynamics modeling of gas-particle flow within a solid-particle solar receiver. *Journal of Solar Energy Engineering, Transactions of the ASME*, *129*(2), 160–170. https://doi.org/10.1115/1.2716418

Cheng, Y. S. (2014). Mechanisms of pharmaceutical aerosol deposition in the respiratory tract. *AAPS PharmSciTech*, *15*(3), 630–640. https://doi.org/10.1208/s12249-014-0092-0

Costa, A. P., Xu, X., Khan, M. A., & Burgess, D. J. (2016). Liposome Formation Using a Coaxial Turbulent Jet in Co-Flow. *Pharmaceutical Research*, *33*(2), 404–416. https://doi.org/10.1007/s11095-015-1798-8

Elghobashi, S. (1994). On predicting particle-laden turbulent flows. *Applied Scientific Research*, *52*(4), 309–329. https://doi.org/10.1007/BF00936835

Elghobashi, S. (2006). An updated classification map of particle-laden turbulent flows. *Fluid Mechanics and Its Applications*, *81*, 3–10.

Faust, S., Goschütz, M., Kaiser, S. A., Dreier, T., & Schulz, C. (2014). A comparison of selected organic tracers for quantitative scalar imaging in the gas phase via laser-induced fluorescence. *Applied Physics B: Lasers and Optics*, *117*(1), 183–194. https://doi.org/10.1007/s00340-014-5818-x

Freund, J. B. (2001). Noise sources in a low-Reynolds-number turbulent jet at Mach 0.9. *Journal of Fluid Mechanics*, *438*, 277–305. https://doi.org/10.1017/S0022112001004414

Gai, G., Hadjadj, A., Kudriakov, S., Mimouni, S., & Thomine, O. (2021). Numerical Study of Spray-Induced Turbulence Using Industrial Fire-Mitigation Nozzles. *Energies*, *14*(4), 1135. https://doi.org/10.3390/en14041135

Gillandt, I., Fritsching, U., & Bauckhage, K. (2001). Measurement of phase interaction in dispersed gas/particle two-phase flow. *International Journal of Multiphase Flow*, *27*(8), 1313–1332. https://doi.org/10.1016/S0301-9322(01)00007-6

Grant, G., Brenton, J., & Drysdale, D. (2000). Fire suppression by water sprays. *Progress in Energy and Combustion Science*, *26*(2), 79–130. https://doi.org/10.1016/S0360-1285(99)00012-X

Greenshields, C. (2011). *OpenFOAM The OpenFOAM Foundation User Guide*. *June*. http://openfoam.org

Hardalupas, Y. (1989). *Velocity and particle-flux characteristics of tu rb u len t particle-laden jets*. *78*(November), 185–195.

Innocenti, A., Marchioli, C., & Chibbaro, S. (2016). Lagrangian filtered density function for LES-based stochastic modelling of turbulent particle-laden flows. *Physics of Fluids*, *28*(11), 115106. https://doi.org/10.1063/1.4967800

Iqbal, N., Rauh, C., & Delgado, A. (2015). Numerical simulations of particle-laden jet/spout flows using Eulerian-Lagrangian approach. *Procedia Engineering*, *102*, 867–876. https://doi.org/10.1016/j.proeng.2015.01.207

Jenny, P., Roekaerts, D., & Beishuizen, N. (2012). Modeling of turbulent dilute spray combustion. *Progress in Energy and Combustion Science*, *38*(6), 846–887. https://doi.org/10.1016/j.pecs.2012.07.001

Kalt, Peter A.M., & Nathan, G. J. (2007). Corrections to facilitate planar imaging of particle concentration in particle-laden flows using Mie scattering. Part 2: Diverging laser sheets. *Applied Optics*, *46*(29), 7227–7236. https://doi.org/10.1364/AO.46.007227

Kirchmann, J., Kronenburg, A., Stein, O. T., & Cleary, M. J. (2020). Two-phase sparse-Lagrangian MMC-LES of dilute ethanol spray flames. *Proceedings of the Combustion Institute*, *000*, 1–8. https://doi.org/10.1016/j.proci.2020.05.009

Kloeden, P. E., Platen, E., & Hofmann, N. (1995). Extrapolation Methods for the Weak Approximation of Ito Diffusions. *SIAM Journal on Numerical Analysis*, *32*(5), 1519–1534. https://doi.org/10.1137/0732069

Lau, T. C. W., & Nathan, G. J. (2014). Influence of Stokes number on the velocity and concentration distributions in particle-laden jets. *Journal of Fluid Mechanics*, *757*(6), 432–457. https://doi.org/10.1017/jfm.2014.496

Lau, T. C. W., & Nathan, G. J. (2016). The effect of Stokes number on particle velocity and concentration distributions in a well-characterised, turbulent, co-flowing two-phase jet. *Journal of Fluid Mechanics*, *809*, 72–110. https://doi.org/10.1017/jfm.2016.666

Lewis, E. W., Lau, T. C. W., Sun, Z., Alwahabi, Z. T., & Nathan, G. J. (2020). Luminescence interference to two-colour toluene laser-induced fluorescence thermometry in a particle-laden flow. *Experiments in Fluids*, *61*(4), 1–16. https://doi.org/10.1007/s00348-020-2942-8

Loth, E. (2008). Drag of non-spherical solid particles of regular and irregular shape. *Powder Technology*, *182*(3), 342–353. https://doi.org/10.1016/j.powtec.2007.06.001

M. Kuerten, J. G. (2016). Point-Particle DNS and LES of Particle-Laden Turbulent flow - a state-of-the-art review. *Flow, Turbulence and Combustion*, *97*(3), 689–713. https://doi.org/10.1007/s10494-016-9765-y

Ma, B., Kourmatzis, A., Zhao, Y., Yang, R., Chan, H.-K., Salehi, F., & Cheng, S. (2020). Potential effects of lingual fats on airway flow dynamics and particle deposition. *Aerosol Science and Technology*, *54*(3), 321–331. https://doi.org/10.1080/02786826.2019.1696014

Maxey, M. R., & Riley, J. J. (1983). Equation of motion for a small rigid sphere in a nonuniform flow. *Physics of Fluids*, *26*(4), 883–889. https://doi.org/10.1063/1.864230

Mergheni, M. A., Sautet, J. C., Godard, G., Ben Ticha, H., & Ben Nasrallah, S. (2009). Experimental investigation of turbulence modulation in particle-laden coaxial jets by Phase Doppler Anemometry. *Experimental Thermal and Fluid Science*, *33*(3), 517–526. https://doi.org/10.1016/j.expthermflusci.2008.11.004

Mi, J., Nobes, D. S., & Nathan, G. J. (2001). Influence of jet exit conditions on the passive scalar

field of an axisymmetric free jet. *Journal of Fluid Mechanics*, *432*(May), 91–125. https://doi.org/10.1017/s0022112000003384

Minier, J. P. (2015). On Lagrangian stochastic methods for turbulent polydisperse two-phase reactive flows. *Progress in Energy and Combustion Science*, *50*, 1–62. https://doi.org/10.1016/j.pecs.2015.02.003

Minier, J. P., Chibbaro, S., & Pope, S. B. (2014). Guidelines for the formulation of Lagrangian stochastic models for particle simulations of single-phase and dispersed two-phase turbulent flows. *Physics of Fluids*, *26*(11). https://doi.org/10.1063/1.4901315

Minier, J. P., & Peirano, E. (2001). The pdf approach to turbulent polydispersed two-phase flows. *Physics Report*, *352*(1–3), 1–214. https://doi.org/10.1016/S0370-1573(01)00011-4

Mostafa, A. A., Mongia, H. C., McDonell, V. G., & Samuelsen, G. S. (1990). An experimental and numerical study of particle-laden coaxial jet flows. *International Journal of Heat and Fluid Flow*, *11*(2), 90–97. https://doi.org/10.1016/0142-727X(90)90001-R

Oefelein, J. C., Sankaran, V., & Drozda, T. G. (2007). Large eddy simulation of swirling particle-laden flow in a model axisymmetric combustor. *Proceedings of the Combustion Institute*, *31 II*, 2291–2299. https://doi.org/10.1016/j.proci.2006.08.017

Pakseresht, P., & Apte, S. V. (2019). Volumetric displacement effects in Euler-Lagrange LES of particle-laden jet flows. *International Journal of Multiphase Flow*, *113*, 16–32. https://doi.org/10.1016/j.ijmultiphaseflow.2018.12.013

Papadopoulos, G., & Pitts, W. M. (1998). Scaling the near-field centerline mixing behavior of axisymmetric turbulent jets. *AIAA Journal*, *36*(9), 1635–1642. https://doi.org/10.2514/2.565

Perrotta, A., Capone, A., & Romano, G. P. (2020). Heavy particles in the near field of a turbulent jet. *European Journal of Mechanics, B/Fluids*, *83*, 156–163. https://doi.org/10.1016/j.euromechflu.2020.04.008

Picano, F., Sardina, G., Gualtieri, P., & Casciola, C. M. (2010). Anomalous memory effects on transport of inertial particles in turbulent jets. *Physics of Fluids*, *22*(5), 1–4. https://doi.org/10.1063/1.3432439

Pope. (1985). PDF methods for turbulent reactive flows. *Progress in Energy and Combustion Science*, *11*(2), 119–192. https://doi.org/10.1016/0360-1285(85)90002-4

Pozorski, J., & Apte, S. V. (2009). Filtered particle tracking in isotropic turbulence and stochastic modeling of subgrid-scale dispersion. *International Journal of Multiphase Flow*, *35*(2), 118–128. https://doi.org/10.1016/j.ijmultiphaseflow.2008.10.005

Prevost, F., Boree, J., Nuglisch, H. J., & Charnay, G. (1996). Measurements of fluid/particle correlated motion in the far field of an axisymmetric jet. *International Journal of Multiphase Flow*, *22*(4), 685–701. https://doi.org/10.1016/0301-9322(96)00009-2

Raman, V., & Pitsch, H. (2007). A consistent LES/filtered-density function formulation for the simulation of turbulent flames with detailed chemistry. *Proceedings of the Combustion Institute*, *31 II*, 1711–1719. https://doi.org/10.1016/j.proci.2006.07.152

Ramkrishna, D. (1985). THE STATUS OF POPULATION BALANCES Doraiswami Ramkrishna. *Reviews in Chemical Engineering*, 49–95. http://www.degruyter.com/dg/viewarticle.fullcontentlink:pdfeventlink/$002fj$002frevce.1985.3.1$002frevce.1985.3.1.49$002frevce.1985.3.1.49.pdf?t:ac=j$002frevce.1985.3.1$002frevce.1985.3.1.49$002frevce.1985.3.1.49.xml

Riber, E., Moureau, V., García, M., Poinsot, T., & Simonin, O. (2009). Evaluation of numerical strategies for large eddy simulation of particulate two-phase recirculating flows. *Journal of Computational Physics*, *228*(2), 539–564. https://doi.org/10.1016/j.jcp.2008.10.001

Rigopoulos, S. (2007). PDF method for population balance in turbulent reactive flow. *Chemical Engineering Science*, *62*(23), 6865–6878. https://doi.org/10.1016/j.ces.2007.05.039

Rigopoulos, S. (2010). Population balance modelling of polydispersed particles in reactive flows. *Progress in Energy and Combustion Science*, *36*(4), 412–443. https://doi.org/10.1016/j.pecs.2009.12.001

Salehi, F., Cleary, M. J., & Masri, A. R. (2017). Population balance equation for turbulent polydispersed inertial droplets and particles. *Journal of Fluid Mechanics*, *831*, 719–742. https://doi.org/10.1017/jfm.2017.653

Salehi, F., Cleary, M. J., Masri, A. R., & Kronenburg, A. (2018). One-way and Two-way Coupled PDF-PBE / LES Simulations of Turbulent Particle-Laden Flows. *Proceedings of the 21st Australasian Fluid Mechanics Conference, AFMC 2018*, *December*, 4–7.

Salehi, F., Cleary, M. J., Masri, A. R., & Kronenburg, A. (2019). PDF-PBE modelling of polydisperse inertial particles in a turbulent recirculating flow. *International Journal of Multiphase Flow*, *117*, 42–52. https://doi.org/10.1016/j.ijmultiphaseflow.2019.04.028

Salehi, F., Cleary, M. J., Masri, A. R., & Kronenburg, A. (2020). Large eddy simulation of polydispersed inertial particles using two-way coupled PDF-PBE. *International Journal of Heat and Fluid Flow*, *83*(October 2019), 108585. https://doi.org/10.1016/j.ijheatfluidflow.2020.108585

Sandberg, R. D., Sandham, N. D., & Suponitsky, V. (2012). DNS of compressible pipe flow exiting into a coflow. *International Journal of Heat and Fluid Flow*, *35*, 33–44. https://doi.org/10.1016/j.ijheatfluidflow.2012.01.006

Sautet, J. C., & Stepowski, D. (1995). Dynamic behavior of variable-density, turbulent jets in their near development fields. *Physics of Fluids*, *7*(11), 2796–2806. https://doi.org/10.1063/1.868658

Smagorinsky, J. (1963). General Circulation Experiments With the Primitive Equations. *Monthly Weather Review*, *91*(3), 99–164. https://doi.org/10.1175/1520-0493(1963)091<0099:gcewtp>2.3.co;2

Sommerfeld, M., Van, W. B., & Oliemans, R. (2008). *Best practice guidelines for computational fluid dynamics of dispersed multiphase flows*. European Research Community on Flow, Turbulence and Combustion.

Sporleder, F., Borka, Z., Solsvik, J., & Jakobsen, H. A. (2012). On the population balance equation. *Reviews in Chemical Engineering*, *28*(2–3), 149–169. https://doi.org/10.1515/revce-2011-0013

Subramaniam, S. (2013). Lagrangian-Eulerian methods for multiphase flows. *Progress in Energy and Combustion Science*, *39*(2–3), 215–245. https://doi.org/10.1016/j.pecs.2012.10.003

Tan, T., & Chen, Y. (2010). Review of study on solid particle solar receivers. *Renewable and Sustainable Energy Reviews*, *14*(1), 265–276. https://doi.org/10.1016/j.rser.2009.05.012

TOWNSEND, A. A. (1976). *THE STRUCTURE OF TURBULENT SHEAR FLOW*.

Varaksin, A. Y., & Polyakov, A. F. (1999). Capabilities and limitations of laser doppler anemometers in studying heterogeneous flows with solid bidisperse particles. *Measurement Techniques*, *42*(9), 888–893. https://doi.org/10.1007/BF02504270

Yarin, L. P., & Hetsroni, G. (1994a). Turbulence intensity in dilute two-phase flows—1 Effect of particle-size distribution on the turbulence of the carrier fluid. *International Journal of Multiphase Flow*, *20*(1), 1–15. https://doi.org/10.1016/0301-9322(94)90002-7

Yarin, L. P., & Hetsroni, G. (1994b). Turbulence intensity in dilute two-phase flows—2 Temperature fluctuations in particle-laden dilute flows. *International Journal of Multiphase Flow*, *20*(1), 17–25. https://doi.org/10.1016/0301-9322(94)90003-5

Yarin, L. P., & Hetsroni, G. (1994c). Turbulence intensity in dilute two-phase flows—3 The particles-turbulence interaction in dilute two-phase flow. *International Journal of Multiphase Flow*, *20*(1), 27–44. https://doi.org/10.1016/0301-9322(94)90004-3

Zhang, J., Lei, Y., & Zhou, L. (2004). Simulation of coaxial jet interactions in a swirl combustor. *Combustion Science and Technology*, *176*(1), 23–43. https://doi.org/10.1080/00102200490255389

Zoltani, C. K., & Bicen, A. F. (1990). *Velocity measurements in a turbulent, dilute, two-phase jet*. *300*, 1986–1989. https://link.springer.com/content/pdf/10.1007/BF00233131.pdf